
CoNO: Complex Neural Operator for Continuous Dynamical Physical Systems

Anonymous Author(s)

Affiliation

Address

email

Abstract

1 Neural operators extend data-driven models to map between infinite-dimensional
2 functional spaces. While these operators perform effectively in either the time
3 or frequency domain, their performance may be limited when applied to non-
4 stationary spatial or temporal signals whose frequency characteristics change with
5 time. Here, we introduce a Complex Neural Operator (CoNO) that parameterizes
6 the integral kernel using Fractional Fourier Transform (FrFT), better representing
7 non-stationary signals in a complex-valued domain. Theoretically, we prove the
8 universal approximation capability of CoNO. We perform an extensive empirical
9 evaluation of CoNO on seven challenging partial differential equations (PDEs),
10 including regular grids, structured meshes, and point clouds. Empirically, CoNO
11 consistently attains state-of-the-art performance, showcasing an average relative
12 gain of 10.9%. Further, CoNO exhibits superior performance, outperforming all
13 other models in additional tasks such as zero-shot super-resolution and robustness to
14 noise. CoNO also exhibits the ability to learn from small amounts of data—giving
15 the same performance as the next best model with just 60% of the training data.
16 Altogether, CoNO presents a robust and superior model for modeling continuous
17 dynamical systems, providing a fillip to scientific machine learning.

18 1 Introduction

19 Continuum systems span various scientific and engineering fields, such as robotics, biological systems,
20 climate modeling, and fluid dynamics, among others [16]. These systems are represented using
21 Partial Differential Equations (PDEs), the solution of which provides the system’s time evolution. The
22 solution of PDEs necessitates the identification of an optimal solution operator, which maps across
23 functional spaces while including the initial conditions and coefficients. Traditionally, numerical
24 methods, such as finite element and spectral methods, have been employed to approximate the
25 solution operator for PDEs. However, these approaches often incur high computational costs and
26 exhibit limited adaptability to arbitrary resolutions and geometries [59]. Such high computational
27 costs of these numerical methods inhibit the real-time prediction crucial in weather forecasting and
28 robotics.

29 Recently, in the realm of scientific machine learning, neural networks present a promising alternative
30 to solve PDEs through a data-driven approach. Specifically, neural operators represent an extension of
31 neural networks, facilitating the mapping between infinite-dimensional functional spaces and serving
32 as a universal approximation of the operator. Notably, these operators learn the functionals without
33 any prior knowledge of the underlying PDE, relying solely on data-driven training, leading to faster
34 inference times than the traditional methods [43, 37].

35 Among different neural operators, the Fourier Neural Operator (FNO) [43] has gained widespread
36 recognition due to its ability to navigate the infinite-dimensional functional space via kernel integral
37 operations in the Fourier domain. Renowned for its versatility, FNO has found successful applications

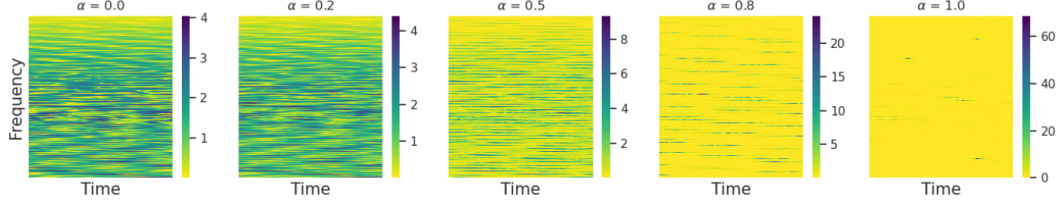


Figure 1: FrFT heatmaps illustrating the temporal-frequency characteristics of the 2D Navier-Stokes equation for varying values of α . Each subplot represents the magnitude of the transformed frequency content over time, obtained by applying the FrFT and then flattened 2D frequency map of the Navier-Stokes equation. Different subplots correspond to fractional orders α , highlighting the diverse spectral behaviors captured by the FrFT across both the temporal and frequency domains. Note that $\alpha = 0$ represents the time domain while $\alpha = 1$ represents the frequency domain.

across diverse domains, including weather forecasting [38], biomedical surrogate modeling [25], and expediting sampling processes in diffusion models [76]. Nevertheless, recent investigations have brought to light some specific challenges associated with FNO, including aliasing errors [19], a departure from continuous-discrete equivalence [6], susceptibility to vanishing gradient problems with an increasing number of layers [61] and susceptibility to poor performance when presented with noisy data [9]. FNO also exhibits suboptimal performance on time-dependent PDEs [42, 9] exemplified by the turbulent Navier-Stokes equations (chaotic flow). Notably, FNO encounters difficulties in making predictions over extended time horizons, constrained by the limitations of the Fourier Transform (FT), which is tailored for stationary signals and needs more time-frequency characteristics—as it decomposes the function based on monochromatic basis function and is unable to detect oscillatory patterns present in chirps signal [60]. For instance, the change of frequency with time in the Navier-Stokes equation is non-stationary and nonlinear (see Fig. 1 and App. Fig. 6), leading to the concentration of spectrum around low frequency in the Fourier Transform. Note that the Navier-Stokes equation holds significant relevance across diverse practical domains, including but not limited to aerodynamics, weather forecasting, and oceanography. Addressing these challenges through a data-driven methodology underscores the pressing need for alternative operator formulation that has ability to learn non-stationary signals.

A generalization of the FT for non-stationary signals, where spectra evolve with time, by employing fractional FT (FrFT) can potentially improve the prediction of long-horizon dynamics, particularly in handling highly nonlinear and rapidly changing time-frequency characteristics [12]. FrFT improves the efficiency of the classical FT by using a general parameterized adjustable orthonormal basis. This basis allows us to break down a chirp function into simpler parts. The adjustable parameter helps efficiently reconstruct the chirp functions [60]. The FrFT generalizes FT by rotating the signal between the time and frequency domains, transitioning from real to complex domain, and incorporating phase information [53], resulting in a complex representation of the signal. However, the complex-valued representations have remained unexplored in the operator learning paradigm which can model the relationships between different parts of the vector field through complex, correlated interactions [8]., although a large literature exists on complex-valued neural networks (CVNNs) [50]. CVNNs offer easier optimization [50], faster convergence during training [4, 15, 70], better generalization [31], data efficiency, and resilience to noise [15, 70]. Thus, combining the operator paradigm with CVNNs can potentially result in an architecture that exploits both best, leading to a model that provides improved long-horizon prediction.

Our Contributions. Motivated by the above observations, we introduce the Complex Neural Operator (CoNO). The major contributions of the present work are as follows.

1. **Novel architecture.** CoNO represents the first instance that performs operator learning employing a CVNN that parameterizes the integral kernel through FrFT, enabling richer information through phase details learnable by CVNNs suitable for non-stationary signals. Table 1 shows the comprehensive comparison of CoNO with current SOTA operators.
2. **Universal approximation.** We prove theoretically that CoNO follows the universal approximation theorem for operators (see Thm 4.3).
3. **Superior performance.** We show that CoNO consistently exhibits superior performance compared to SOTA operators, always ranking among the top two on all the datasets with an average gain of 10.9% as presented in Table 2.

4. **Data efficiency and robustness to noise.** CoNO demonstrates superior performance even with limited samples, data instances, and training epochs. CoNO provides more robustness when noise is injected into the training data compared to the existing methods and performs better than SOTA methods even under 0.1% data noise.

2 Related Work

Neural Operators (NO): Neural operators have shown promise in solving PDEs in a data-driven fashion [37]. Lu et al. [47] introduced DeepOnet, theoretically establishing its universal approximation capabilities. The DeepOnet architecture comprises a branch network and a trunk network, with the former dedicated to learning the input function operator and the latter tasked with learning the function space onto which it is projected. Another famous architecture, the FNO, proposed by Li et al. [43], utilizes a frequency domain method. FNO incorporates Fourier kernel-based integral transformations through fast Fourier transform and projection blocks. An enhanced version, F-FNO [61], improves upon the original FNO by integrating distinct spectral mixing and residual connections. Subsequently, various kernel integral neural operators based on transformations have emerged. For example, Fanaskov and Oseledets [19] introduced spectral methods, such as Chebyshev and Fourier series, to mitigate aliasing errors and enhance clarity in FNO outputs. Li et al. [44] incorporated specialized learnable transforms to facilitate operator learning on irregular domains, achieved by transforming them into uniform latent meshes.

Kovachki et al. [37] demonstrated that the well-known attention mechanism can be seen as a particular case of neural operator learning the integral kernel specifically applied to address irregular meshes for solving PDEs, a characteristic managed by Geo-FNO [44] differently. Cao [11] employed two self-attention mechanism-based operators without utilizing a softmax layer, accompanied by a theoretical interpretation. Recently, Hao et al. [27] introduced the GNOT operator, featuring a linear cross-attention block designed to enhance the encoding of irregular geometries. However, transformer-based operators are susceptible to issues arising from limited data samples, displaying a tendency to overfit easily on training data without exhibiting robust generalization. In addressing the challenges posed by multiscale PDEs, Liu et al. [45] proposed a hierarchical attention-based operator.

Fractional Fourier Transform (FrFT): The FrFT represents a generalization of the classical Fourier Transform (FT), providing robust capabilities for spectral analysis. It achieves this by facilitating the transformation of input signals into an intermediate domain between the time and frequency domains, thereby establishing a time-frequency representation [53]. FrFT is particularly effective in processing non-stationary signals, commonly called "chirp signals" or signals exhibiting frequency derivatives over time. App. Fig. 7 illustrates the efficacy of employing the FrFT for noise filtering within the signal spectrum through the rotation of the fractional order axis. In contrast to FrFT, alternative signal processing techniques such as wavelet or Gabor transformation don't provide a joint signal energy distribution across both time and frequency domains. Additionally, these alternatives often grapple with challenges related to high computational complexity, the selection of wavelet functions, and sensitivity to signal noise. FrFT, with its distinct advantages, has found applications in various domains, ranging from solving differential equations [48], wireless communication [41], biomedical signal processing [24], image encryption and image compression [49] etc. Yu et al. [75] demonstrated the benefits of employing FrFT over conventional convolution across various tasks in computer vision, including segmentation, object detection, classification, super-resolution, etc.

Complex Valued Neural Networks (CVNNs): A CVNN incorporates complex-valued parameters and variables within its architecture, enabling the representation of both magnitude and phase information in the neural networks [39, 14]. The utilization of CVNNs encompasses diverse advantages, extending from biological to signal processing applications. Danihelka et al. [15] has demonstrated that complex numbers enhance efficiency and stability in information retrieval processes. Additionally, Arjovsky et al. [4] have introduced complex recurrent neural networks (RNNs), highlighting that unitary matrices offer a more intricate representation, thereby mitigating issues associated with vanishing and exploding gradient problems. In image processing, phase information is a critical descriptor, offering detailed insights about image shape, orientation, and edges. Oppenheim and Lim

Table 1: A comprehensive comparative analysis of features of state-of-the-art operators with CoNO. "*" denotes not applicable.

Features	FNO	LSM	CoNO (Ours)
Integral Kernel	Frequency	Spatial	Spatial-Frequency
Elementary function	Sine	*	Linear Frequency Modulation
Representation	Real	Real	Complex
Pertinent Signal	Stationary	*	Time Varying Signal
α Parameter	Fixed (90°)	Fixed (0°)	Not Fixed (Learnable)
Applicability	Individual	Individual	Unified

[52] showed the information encapsulated in the phase of an image proves sufficient for the recovery of a substantial proportion of the encoded magnitude information.

CVNNs have been a research focus for a long time [21, 33, 30, 51]. Recently, Geuchen et al. [23] established the universal approximation capabilities of CVNNs for deep, narrow architectures, significantly contributing to understanding their expressive power. Prior works [57, 64, 4, 15, 13, 22] have made noteworthy strides in both experimental and theoretical aspects of CVNNs. In the domain of computer vision, the utilization of scattering transformation-based complex neural networks has demonstrated considerable promise, showcasing their ability to achieve performance on par with real-valued counterparts while employing significantly fewer parameters [35, 71, 56]. In NLP, complex embeddings have been incorporated for semantic and phonetic processing of natural languages [63, 17]. In contrast, Yang et al. [74] and Dong et al. [18] showcased the advantages of employing CVNNs transformers for the NLP community. Despite these notable applications across various domains, exploring the applicability of CVNNs within the SciML community is still limited.

3 Preliminaries

Problem Setting: We have followed and adopted the notations in Li et al. [43]. Let D denote a bounded open set as $D \subset \mathbb{R}^d$, with $A = A(D; \mathbb{R}^{d_a})$ and $U = U(D; \mathbb{R}^{d_u})$ as separable Banach spaces of functions representing elements in \mathbb{R}^{d_a} and \mathbb{R}^{d_u} , respectively. Consider $\mathcal{G}^\dagger : A \rightarrow U$ to be a nonlinear surrogate mapping arising from the solution operator for a parametric PDE. It is assumed that there is access to i.i.d. observations $(a_j, u_j)_{j=1}^N$, where $a_j \sim \mu$, drawn from the underlying probability measure μ supported on A , and $u_j = \mathcal{G}^\dagger(a_j)$.

The objective of operator learning is to construct an approximation for \mathcal{G}^\dagger via a parametric mapping $\mathcal{G} : A \times \Theta \rightarrow U$, or equivalently, $\mathcal{G}_\theta : A \rightarrow U, \theta \in \Theta$, within a finite-dimensional parameter space Θ . The aim is to select $\theta^\dagger \in \Theta$ such that $\mathcal{G}(\cdot, \theta^\dagger) = \mathcal{G}_\theta^\dagger \approx \mathcal{G}^\dagger$. This framework facilitates learning in infinite dimensional spaces as the solution to the optimization problem in Eq. 1 constructed using a loss function $\mathcal{L} : U \times U \rightarrow \mathbb{R}$.

$$\min_{\theta \in \Theta} \mathbb{E}_{a \sim \mu} [\mathcal{L}(\mathcal{G}(a, \theta), \mathcal{G}^\dagger(a))], \quad (1)$$

The optimization problem is solved in operator learning frameworks using a data-driven empirical approximation of the loss function akin to the regular supervised learning approach using train-test observations. Usually, \mathcal{G}_θ is parameterized using deep neural networks.

Fractional Fourier Transform (FrFT): Inspired by the kernel formulation for solving linear PDEs using Green’s function, we construct the model \mathcal{G}_θ employing an iterative approach to map an input function a to an output function u within the CoNO framework as detailed in Sec. 4. In CoNO, the kernel integral is formulated using the FrFT with a learnable order. The fractional transformation of order α ($\alpha \in \mathbb{R}$) is a parameter of the Fractional Fourier Transform (FrFT) that corresponds to the α^{th} power of the Fourier Transform (FT) (denote by \mathcal{F}^α).

Definition 3.1 (FrFT). The fractional Fourier transform with angle α of a signal $f(y)$ is defined as:

$$\mathcal{F}^\alpha(f)(m) = \int_{-\infty}^{\infty} f(y) \mathcal{K}_\alpha(m, y) dy, \quad (2)$$

where,

$$\mathcal{K}_\alpha(m, y) = \begin{cases} c(\alpha) \exp\{j\pi a(\alpha)[(m^2 + y^2) - 2b(\alpha)my]\} & \text{if } \alpha \neq n\pi\mathbb{Z}, \\ \delta(m - y) & \text{if } \alpha = 2\pi\mathbb{Z}, \\ \delta(m + y) & \text{if } \alpha + \pi = 2\pi\mathbb{Z} \end{cases}$$

where, $a(\alpha) = \cot \alpha$, $b(\alpha) = \csc \alpha$, and $c(\alpha) = \sqrt{1 - j \cot \alpha}$ and $\mathcal{F}^\alpha(f)(m)$ denotes the m^{th} fractional fourier coefficient of order α of f .

Remark 3.2. For Eq. 2, it reduces to **Standard Fourier Transform (FT)** when $\alpha = \frac{\pi}{2}$, then $\cot \alpha = 0$ and $\csc \alpha = 1$.

Complex Valued Neural Networks (CVNNs): In the CoNO framework, the integration of kernels in the operator \mathcal{G}_θ is performed within the complex-valued domain using CVNNs. A CVNN is modeled as real and imaginary parts or magnitude and phases as follows [63]:

$$z = x + jy = |z|e^{j\angle z} \quad (3)$$

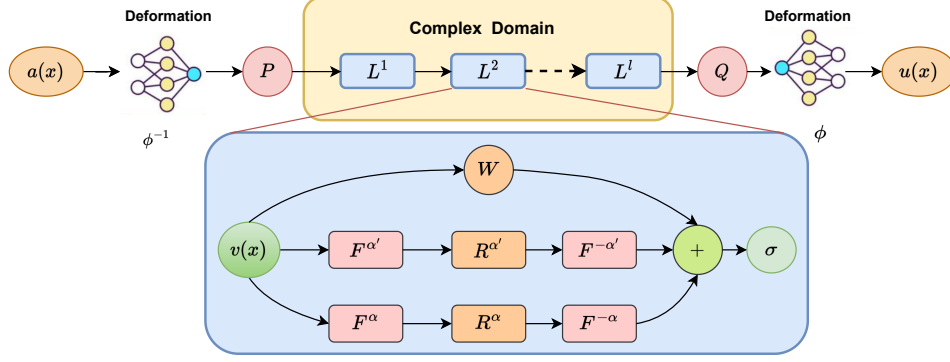


Figure 2: **CoNO Architecture Overview.** (Top) (1) The input function $a(x)$ undergoes a deformation ϕ^{-1} to convert an irregular mesh into a uniform mesh. (2) The deformed input is then lifted to a higher dimension in the channel space using a neural network. (3) Apply iterative CoNO layer in complex domain consisting of fractional integral kernel. (4) Then, the output is projected back on the lower dimension in channel space using neural network. (5) Solution $u(x)$ is obtained by passing through the deformation ϕ . (Bottom) Zoomed version of FrFT integral kernel defined in Eq. 6 with learnable parameters R^α , $R^{\alpha'}$, W and fractional order α and α' .

181 where $j = \sqrt{-1}$ is imaginary unit, x and y are the real and imaginary parts of z , and $|z|$ and $\angle z$ are
 182 the magnitude and phase of z .

183 **Definition 3.3** (Complex Valued Activation). Let $z \in \mathbb{C}$ be a complex number with real part $\text{Re}(z)$
 184 and imaginary part $\text{Im}(z)$. The Complex GeLU (CGeLU) activation function is defined as follows:

$$\text{CGeLU}(z) = \text{GeLU}(\text{Re}(z)) + j \cdot \text{GeLU}(\text{Im}(z)), \quad (4)$$

185 where $\text{GeLU}(\cdot)$ is the Gaussian Error Linear Unit activation function [29]. The CGeLU activation
 186 function satisfies the Cauchy-Riemann equations when the real and imaginary parts of z are strictly
 187 positive or negative.

188 **Complex Valued Back-propagation:** Complex-valued back-propagation involves extending tradi-
 189 tional back-propagation algorithms to handle complex numbers, utilizing mathematical tools like
 190 Wirtinger calculus [3] which enable training neural networks with complex-valued weights and
 191 activation, allowing for the modeling of intricate relationships within complex data domains [5, 14].

192 4 Complex Neural Operator (CoNO)

193 4.1 Proposed Method

194 Here, we introduce our framework, named the Complex Neural Operator (CoNO) depicted in Fig. 2.

195 **Overview:** Suppose \mathcal{G}_θ represents an iterative sequence of functions. The operator $\mathcal{G}_\theta : A \rightarrow U$,
 196 where $A = A(D; \mathbb{R}^{d_a})$ and $U = U(D; \mathbb{R}^{d_u})$ are separable Banach spaces of functions, represent-
 197 ing elements in \mathbb{R}^{d_a} and \mathbb{R}^{d_u} , respectively. Our goal is to construct the operator in a structure-
 198 preserving manner where we band-limit a function over a given spectrum [66], thus preserving com-
 199 plex continuous-discrete equivalence such that Shannon-Whittaker-Kotel'nikov theorem is obeyed for
 200 all continuous operations [65]. With this, our operator CoNO, denoted by \mathcal{G}_θ is defined as follows:

$$\mathcal{G}_\theta = \phi \circ \mathcal{Q} \circ \mathcal{L}_l \circ \dots \circ \mathcal{L}_1 \circ \mathcal{P} \circ \phi^{-1}, \quad (5)$$

201 where \circ denotes composition. On irregular geometries, ϕ represents the function modeled by a neural
 202 network that maps the irregular domain into a regular latent mesh for operator learning. The operators
 203 $\mathcal{P} : \mathbb{R}^{d_a} \rightarrow \mathbb{R}^{d_1}$ and $\mathcal{Q} : \mathbb{R}^{d_1} \rightarrow \mathbb{R}^{d_u}$ correspond to the lifting and projection operations, encoding
 204 lower-dimensional spaces into higher-dimensional spaces or vice versa which helps in converting the
 205 non-linear dynamics into linear dynamics inspired by Koopman Operator [7]. The operator consists
 206 of l layers of non-linear integral operators $\sigma(\mathcal{L}_i)$ (Eq. 6), where σ is an activation function which
 207 is applied from layer \mathcal{L}_i , where i belongs to 1 to $l-1$ to introduce non-linearity in operators, akin
 208 to standard neural networks, to learn highly nonlinear operators, and θ denotes all the learnable
 209 parameters of the operator.

210 **Non-linear Operator Layer, \mathcal{L} :** In CoNO, the complex kernel operator is defined as follows:

$$v^{l+1}(x) = \sigma(Wv^l(x) + b^l + \mathcal{K}(a, \alpha)v^l(x)) \quad \forall x \in D \quad (6)$$

where: v^l is the representation at layer l and $v^l \in \mathbb{C}^{d_l}$, $\mathcal{K} : V^l \times \Theta_K \rightarrow \mathcal{L}(V^{l+1}(D; \mathbb{C}^{d_l}), V^{l+1}(D; \mathbb{C}^{d_{l+1}}))$ maps to bounded linear operators on $V^{l+1}(D; \mathbb{R}^{d_{l+1}})$ as integral operator is linear and bounded operator as shown in App. section B, σ is a non-linear complex activation function, W is a linear transformation, $W : \mathbb{C}^{d_l} \rightarrow \mathbb{C}^{d_{l+1}}$, $\mathcal{K}(a, \phi)$ is an integral kernel parameterized by CVNN (Eq. 7), a is a complex input function, and α belongs to the parameter space of \mathcal{G}_θ and b is the bias.

Fractional Integral Operator, $\mathcal{K}(a, \alpha)$: In CoNO, the integral operator is defined as, $\mathcal{K}(a, \alpha) : V^l(D) \rightarrow V^l(D)$ as follows:

$$\mathcal{K}(a, \alpha)v^l(x) = \sum_{a \in \alpha, \alpha'} \mathcal{F}^{-a}(R^a \cdot (\mathcal{F}^a v^l))(x) \quad \forall x \in D \quad (7)$$

where, \mathcal{F}^α denotes the FrFT with order α , $\mathcal{F}^{-\alpha}$ denotes the inverse FrFT, R^α is the learnable function which we learn from data, a is a complex input function, α is the learnable fractional order which we learn with data as well and α' belongs to the parameter space of \mathcal{G}_θ . **The order α is crucial in determining the optimal spatial-frequency characteristics for analyzing non-stationary signals.** Note that although R^α can be parameterized using a neural network, in the present work, we observed that linear transformation provided slightly better performance than deep neural networks and hence used the same. **In CoNO, we initialized α at approximately 1 to capture the frequency characteristics and α' at around 0.5 to provide a unified spatial-frequency characteristic for non-stationary signals, learned alongside the neural network parameters. However, when α and α' were fixed at 1 and 0.5, respectively, performance was slightly decreased.** In the subsequent subsection, we theoretically prove that the proposed operator can map between infinite-dimensional spaces, leading to the learning of non-linear operators.

4.2 Theoretical Analysis

In this subsection, we present a theoretical analysis of several components of the proposed method. Specifically, we prove the following. (i) The N -dimensional FrFT can be decomposed into one-dimensional FrFT. This decomposition is crucial for CoNO, as it relies on multidimensional FrFT (Thm. 4.1). (ii) Multiplication in the fractional domain is equivalent to convolution in the spatial domain for the proposed operator CoNO (Thm. 4.2). (iii) The universal approximation capability for the CoNO (Thm. 4.3).

Theorem 4.1 (Product Rule for FrFT). *Suppose $\mathcal{K}_\alpha(m_1, x_1, m_2, x_2, \dots, m_n, x_n)$ denote the fractional integral kernel of the N -dimensional FrFT of a signal $f(x_1, x_2, \dots, x_n)$ with m_1, m_2, \dots, m_n denoting the multidimensional FrFT coefficients, then the following fractional kernel property holds:*

$$\mathcal{K}_\alpha(m_1, x_1, m_2, x_2, \dots, m_n, x_n) = \prod_{i=1}^N \mathcal{K}_\alpha(m_i, x_i) \quad (8)$$

Proof. Refer to the App. B.9 for the proof. Thm. 4.1, show that an N -dimensional fractional integral kernel is a product of one-dimensional fractional integral kernels along each dimension.

Theorem 4.2 (Convolution Theorem for FrFT). *Suppose f and g are square-integrable functions. Define $e_\alpha(m) = e^{i\pi|m|^2 \cot(\alpha)}$ and $h(x) = (f * g)(x)$ where $*$ denotes the usual convolution integral with \mathcal{F}^α , \mathcal{G}^α , \mathcal{H}^α respectively denoting the FrFT of f , g and h , respectively. Then,*

$$\mathcal{H}^\alpha(m) = \mathcal{F}^\alpha(m) \mathcal{G}^\alpha(m) e_{-\alpha}(m). \quad (9)$$

Proof. Refer to App. B.12 for the proof. Thm. 4.2 states that the convolution of two functions in the spatial domain is equivalent to the product of their respective fractional Fourier transforms, multiplied by a function dependent on the fractional order.

Finally, we present the universal approximation theorem of CoNO below, similar to that for FNO [36].

Theorem 4.3 (Universal Approximation). *Let $s, s' > 0$ and $\alpha \in \mathbb{R}$; Suppose $\mathcal{G} : H^s(\mathcal{T}_\alpha^d; \mathbb{R}^{d_a}) \rightarrow H^{s'}(\mathcal{T}_\alpha^d; \mathbb{R}^{d_u})$ represent a continuous operator between Sobolev spaces where \mathcal{T}_α^d denotes the fractional order torus and $d_a, d_u \in \mathbb{N}$; and $K \subset H^s(\mathcal{T}_\alpha^d; \mathbb{R}^{d_a})$ is a compact subset. Then, for any $\varepsilon > 0$, there exists CoNO layers $\mathcal{N} : H^s(\mathcal{T}_\alpha^d; \mathbb{R}^{d_a}) \rightarrow H^{s'}(\mathcal{T}_\alpha^d; \mathbb{R}^{d_u})$ satisfying:*

$$\sup_{v \in K} \|\mathcal{G}(v) - \mathcal{N}(v)\|_{L^2} \leq \varepsilon \quad (10)$$

Proof. Refer to App. B.15 for the proof.

Table 2: The main result with sixteen baselines on all benchmarks datasets: Mean Relative ℓ_2 Error (Equation 11) is reported as the evaluation metric, where a smaller ℓ_2 Error indicates superior performance. "INCREMENT %" refers to the relative error reduction concerning the second-best model on each benchmark. Specifically focusing on the 2D Navier–Stokes benchmark, a detailed comparison is conducted with KNO [73], and TF-Net [68], as they are designed for auto-regressive (time-dependent) tasks. Instances marked with '*' indicate that the baseline cannot handle the benchmark. In the color legend, **blue** represents the best performance, **green** indicates the second-best performance, and **orange** signifies the third-best performance among the baselines.

MODEL	Elasticity-P	Elasticity-G	Plasticity	Navier-Stokes	Darcy	Airfoil	Pipe
U-NET [2015]	0.0235	0.0531	0.0051	0.1982	0.0080	0.0079	0.0065
RESNET [2016]	0.0262	0.0843	0.0233	0.2753	0.0587	0.0391	0.0120
TF-NET [2020]	\	\	\	0.1801	\	\	\
SWIN [2021]	0.0283	0.0819	0.0170	0.2248	0.0397	0.0270	0.0109
DEEPONET [2021]	0.0965	0.0900	0.0135	0.2972	0.0588	0.0385	0.0097
FNO [2020]	0.0229	0.0508	0.0074	0.1556	0.0108	0.0138	0.0067
U-FNO [2022]	0.0239	0.0480	0.0039	0.2231	0.0183	0.0269	0.0056
WNO [2022]	0.0334	0.0705	0.0087	0.2763	0.0223	0.0207	0.0098
WMT [2021]	0.0359	0.0520	0.0076	0.1541	0.0082	0.0075	0.0077
GALERKIN [2021]	0.0240	0.1681	0.0120	0.2684	0.0170	0.0118	0.0098
SNO [2022]	0.0390	0.0987	0.0070	0.2568	0.0495	0.0893	0.0294
U-NO [2022]	0.0258	0.0469	0.0034	0.1713	0.0113	0.0078	0.0100
HT-NET [2022]	0.0372	0.0472	0.0333	0.1847	0.0079	0.0065	0.0059
F-FNO [2021]	0.0263	0.0475	0.0047	0.2322	0.0077	0.0078	0.0070
KNO [2023]	\	\	\	0.2023	\	\	\
GNOT [2023]	0.0315	0.0494	*	0.1670	0.0105	0.0081	*
LSM [2023]	0.0218	0.0408	0.0025	0.1535	0.0065	0.0062	0.0050
CoNO (Ours)	0.0210	0.0436	0.0019	0.1287	0.0051	0.0057	0.0054
INCREMENT %	3.8%	-6.8%	31.6%	19.3%	27.5%	8.7%	-8.0%

5 Numerical Experiments

This section provides a thorough empirical investigation of CoNO in contrast to multiple vision models and neural operator baselines. We conduct extensive experiments on a diverse set of challenging benchmarks spanning various domains to demonstrate the efficacy of our proposed method.

5.1 Experiments Details and Main Result

Benchmarks: We assess the performance of our model on Darcy and Navier Stokes [43] benchmarks to gauge its proficiency on regular grids. Subsequently, we extend our experimentation to benchmarks featuring irregular geometries, such as Airfoil, Plasticity, and Pipe [44], modeled using structured meshes and Elasticity [44], represented in point clouds. Refer to App. section C for more details about benchmarks and tasks.

Baselines: We assess CoNO by comparing it against seventeen established models across seven benchmarks, which include baselines from vision models (U-Net [58], ResNet [28], SwinTransformer [46]) and thirteen baselines specifically designed for PDEs (DeepONet [47], TF-Net [68], FNO [43], U-FNO [69], WNO [62], WMT [26], GalerkinTransformer [11], SNO [19], U-NO [54], HT-Net [45], F-FNO [61], KNO [73], GNOT [27], LSM [72]). Notably, for the Elasticity-P benchmark in the point cloud, we incorporate the specialized transformation proposed by geo-FNO [44] at both the start and end of these models. This transformation facilitates the conversion of irregular input domains into or back from a uniform mesh.

Evaluation Metric: Mean relative ℓ_2 error is used throughout the experiments.

$$\mathcal{L} = \frac{1}{N} \sum_{i=1}^N \frac{\|\mathcal{G}_\theta(a_i) - \mathcal{G}^\dagger(a_i)\|_2}{\|\mathcal{G}^\dagger(a_i)\|_2} \quad (11)$$

the regular mean-squared error (MSE) is enhanced with a normalizer $\|\mathcal{G}^\dagger(a_i)\|_2$ to take account for discrepancies in absolute resolution scale across different benchmarks as described in [43].

Implementation Details: We have used mean relative ℓ_2 error (Eq. 11) as the training and evaluation metric. We train all the models for 500 epochs using the Adam optimizer [34]. Comprehensive details are provided in the App. section D. All the experiments are conducted on a Linux machine running Ubuntu 20.04.3 LTS on an Intel(R) Core(TM) i9-10900X processor and a single NVIDIA RTX A6000 GPU with 48 GB RAM.

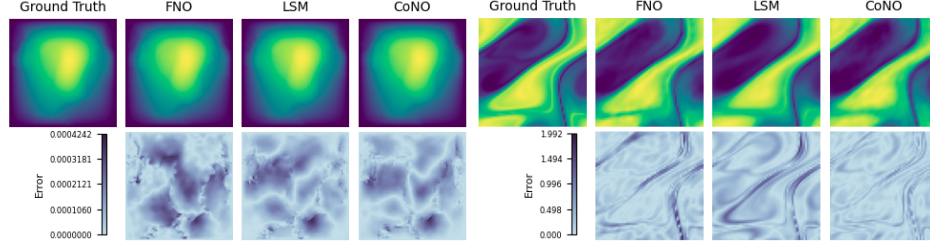


Figure 3: Depiction of results for different methods on fluid datasets, Darcy Flow (**Left**) and Navier Stokes (**Right**). We plotted the heatmap of the absolute difference value between ground truth and prediction to compare the predicted output. See the App. Fig. 10 for more solid physics and fluid physics benchmarks showcases.

Empirical Results: As illustrated in Table 2, CoNO consistently demonstrates superior performance on all the datasets in comparison to all baseline models, ranking among the top two. This performance superiority is evident across benchmark datasets characterized by diverse geometries and dimensions, exhibiting an average improvement of 10.9%. With the second-best performance observed in the Pipe and Elasticity-G benchmarks, our findings suggest that architectures resembling UNET demonstrate superior efficacy in capturing the underlying solution compared to the CoNO model. When applied to time-dependent PDEs, CoNO surpasses all previously established baselines, achieving an average improvement of 25.5%. This result underscores the efficacy of incorporating the change in frequency derivative captured by the FrFT in complex domains, thereby showcasing the promise of our approach in handling temporal dynamics in PDEs.

5.2 Ablation Study and Additional Results

To assess the efficacy of each component in the CoNO operator, we conducted a comprehensive ablation study by systematically excluding individual components. The results presented in Table 3 indicate that all components are crucial for the effectiveness of the CoNO operator, as evidenced by a notable change in the ℓ_2 error with the addition or deletion of an element. Specifically, removing the FrFT block results in a substantial degradation in performance, underscoring its effectiveness in capturing non-stationary signals. Similarly, the absence of the CVNN leads to comparable adverse effects. Notably, our analysis reveals that including bias is instrumental in introducing high-frequency components, further emphasizing its importance. Interestingly, CoNO performance degraded only slightly after removing the alias-free activation function as defined. It raises an intriguing question regarding its necessity for optimizing the operator’s efficiency.

Table 3: Comprehensive ablation study on CoNO: investigating the impact of individual component removal on Navier-Stokes and Darcy Flow benchmark (w/o denotes the performance without that component).

DESIGN	Navier-Stokes	Darcy
w/o Bias	0.1425	0.0080
w/o FrFT	0.1535	0.0086
w/o Complex NN	0.1390	0.0072
w/o Alias Free Activation	0.1295	0.0052
CoNO	0.1287	0.0050

Visual Demonstrations: For a concise representation of intuitive performance, Fig. 3 presents a comparative analysis between FNO, LSM, and CoNO. Notably, CoNO exhibits remarkable proficiency in addressing time-dependent PDEs, including Navier-Stokes and Plasticity, as depicted in App. Fig. 10. Moreover, CoNO outperforms LSM and FNO significantly in the case of Darcy by 27% and having fewer artifacts present in prediction. Additionally, CoNO excels in capturing singularities around corners, as illustrated in the elasticity dataset in the App. Fig. 10, emphasizing its robust and superior performance.

Performance across various Resolutions: In Fig. 4 (Left), the operator CoNO consistently exhibits superior performance compared to other operators on darcy flow PDEs at various resolutions. Notably, CoNO demonstrates stability across different resolutions, adhering to the principle of discrete-continuous equivalence as shown in App. section F.1. It contrasts HT-Net, which experiences degradation in very high dimensions. Furthermore, FNO and CoNO represent the exclusive class of operators capable of zero-shot super-resolution without requiring explicit training.

Out of Distribution Generalization: We conducted experiments on the Navier-Stokes dataset in this investigation, training our model with a viscosity coefficient of 10^{-5} . Subsequently, we assessed

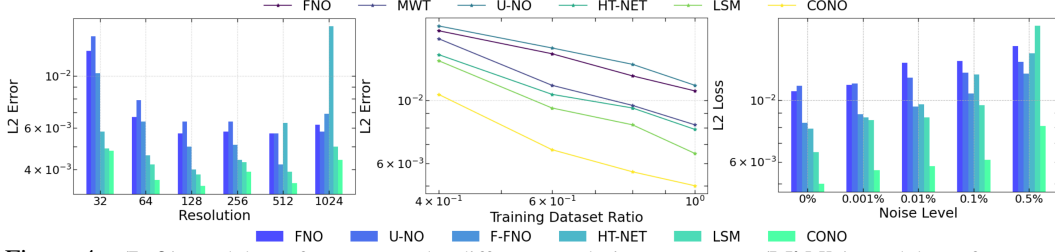


Figure 4: **(Left)** Models performance under different resolutions on Darcy. **(Middle)** Models performance under different training datasets the ratio on Darcy. **(Right)** Models performance under the presence of noise on Darcy. The lower l_2 loss indicates better performance.

the out-of-distribution generalization capabilities by evaluating the trained model on a viscosity coefficient of 10^{-4} . Our findings consistently reveal that CoNO demonstrates a significantly superior generalization performance, exhibiting an increment of 64.3% compared to FNO. It also highlights the significance of capturing latent variable information or the UNET architecture, as achieved by LSM, which outperforms all other operators even CoNO as shown in App. section F.3.

Data Efficiency: As demonstrated in Fig. 4 (Middle), CoNO exhibits comparable performance to the second-best operator LSM when trained on 60% of the data. Furthermore, across various training dataset ratios, CoNO consistently outperforms all other operators, underscoring its superior data efficiency compared to SOTA operators as demonstrated in App. section F.6.

Robustness to Noise: In this study, we performed experiments introducing different noise levels into the training using Gaussian noise. The noise addition process follows: For each input sample denoted as $x(n)$ within the dataset D , we modified it by adding Gaussian noise with parameters $\gamma N(0, \sigma_D^2)$. Here, σ_D^2 represents the variance of the entire dataset, and γ indicates the specified noise intensity level. Our investigation yielded notable results as in Fig. 4 (Right), particularly when evaluating the performance of CoNO in the presence of noise within the training dataset; specifically, the noisy training with 0.1% yielded a better result than the LSM operator without noisy training, confirming the robustness of CoNO to the noisy dataset shown in App. section F.2.

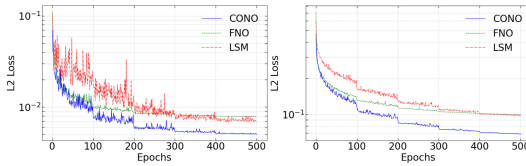


Figure 5: Learning Curve for Darcy flow **(Left)** and Navier Stokes **(Right)** where the x-axis denotes epochs and the y-axis l_2 error.

Training Stability: The performance of CoNO is more stable during training, as visually observed in Fig. 5. The model exhibits reduced oscillations and consistently performs better than FNO and LSM. Remarkably, CoNO attains an equivalent performance compared with the best LSM performance after training within the initial 200 epochs, demonstrating its efficient faster and better convergence while training.

Long Time Prediction on Navier Stokes: We evaluated the long-term behavior of the proposed operator CoNO by training it on the Navier-Stokes equation (viscosity coefficient of 10^{-4}), as shown in the App. section F.5 shows that CoNO excels in extrapolating beyond the prediction horizon compared to LSM and FNO.

6 Conclusion

Altogether, we introduce a new operator learning paradigm called the CoNO, which capitalizes on CVNNs and the FrFT as the integral operator. We theoretically prove that CoNO follows the universal approximation theorem. We demonstrate the effectiveness of leveraging the expressive power of CVNNs within the operator learning framework to construct resilient, data-efficient, and superior neural operators capable of improving the learning of function-to-function mappings. Empirically, we show that CoNO presents the SOTA results in terms of performance, zero-shot super-resolution, out-of-distribution generalization, and noise robustness. This advancement makes CoNO a promising method for developing efficient operators for real-time PDE inference, offering new tools for the SciML community.

Limitations and future work. Although CoNO shows improved empirical performance, the specific features that enable this superiority remain unclear. Understanding the loss landscape and learning mechanisms behind this performance is crucial. Additionally, making CoNO computationally

efficient is essential to accelerate inference. Additional future work and limitations are discussed in App. section G. Further, the broader impacts of the work are discussed in App. section H.

References

- [1] Imtiaz Ahmad, Hijaz Ahmad, Phatiphat Thounthong, Yu-Ming Chu, and Clemente Cesarano. Solution of multi-term time-fractional pde models arising in mathematical biology and physics by local meshless method. *Symmetry*, 12(7):1195, 2020.
- [2] Luís B Almeida. An introduction to the angular fourier transform. In *1993 IEEE International Conference on Acoustics, Speech, and Signal Processing*, volume 3, pages 257–260. IEEE, 1993.
- [3] Md Faijul Amin, Muhammad Ilias Amin, Ahmed Yarub H Al-Nuaimi, and Kazuyuki Murase. Wirtinger calculus based gradient descent and levenberg-marquardt learning algorithms in complex-valued neural networks. In *International Conference on Neural Information Processing*, pages 550–559. Springer, 2011.
- [4] Martin Arjovsky, Amar Shah, and Yoshua Bengio. Unitary evolution recurrent neural networks. In *International conference on machine learning*, pages 1120–1128. PMLR, 2016.
- [5] Jose Agustin Barrachina, Chengfang Ren, Gilles Vieillard, Christele Morisseau, and Jean-Philippe Ovarlez. Theory and implementation of complex-valued neural networks. *arXiv preprint arXiv:2302.08286*, 2023.
- [6] Francesca Bartolucci, Emmanuel de Bézenac, Bogdan Raonić, Roberto Molinaro, Siddhartha Mishra, and Rima Alaifari. Are neural operators really neural operators? frame theory meets operator learning. *arXiv preprint arXiv:2305.19913*, 2023.
- [7] Petar Bevanda, Stefan Sosnowski, and Sandra Hirche. Koopman operator dynamical models: Learning, analysis and control. *Annual Reviews in Control*, 52:197–212, 2021.
- [8] Johannes Brandstetter, Rianne van den Berg, Max Welling, and Jayesh K Gupta. Clifford neural layers for pde modeling. *arXiv preprint arXiv:2209.04934*, 2022.
- [9] Priyanshu Burark, Karn Tiwari, Meer Mehran Rashid, AP Prathosh, and NM Anoop Krishnan. Codbench: A critical evaluation of data-driven models for continuous dynamical systems. *Digital Discovery*, 2024.
- [10] C. Candan, M.A. Kutay, and H.M. Ozaktas. The discrete fractional fourier transform. *IEEE Transactions on Signal Processing*, 48(5):1329–1337, 2000. doi: 10.1109/78.839980.
- [11] Shuhao Cao. Choose a transformer: Fourier or galerkin. *Advances in neural information processing systems*, 34:24924–24940, 2021.
- [12] Eric Chassande-Mottin and Patrick Flandrin. On the time–frequency detection of chirps1. *Applied and Computational Harmonic Analysis*, 6(2):252–281, 1999.
- [13] Soumick Chatterjee, Pavan Tummala, Oliver Speck, and Andreas Nürnberger. Complex network for complex problems: A comparative study of cnn and complex-valued cnn. In *2022 IEEE 5th International Conference on Image Processing Applications and Systems (IPAS)*, pages 1–5. IEEE, 2022.
- [14] Trabelsi Chiheb, O Bilaniuk, D Serdyuk, et al. Deep complex networks. In *International Conference on Learning Representations*, 2017.
- [15] Ivo Danihelka, Greg Wayne, Benigno Uribe, Nal Kalchbrenner, and Alex Graves. Associative long short-term memory. In *International conference on machine learning*, pages 1986–1994. PMLR, 2016.
- [16] Lokenath Debnath and Lokenath Debnath. *Nonlinear partial differential equations for scientists and engineers*. Springer, 2005.
- [17] Caglar Demir and Axel-Cyrille Ngonga Ngomo. Convolutional complex knowledge graph embeddings. In *The Semantic Web: 18th International Conference, ESWC 2021, Virtual Event, June 6–10, 2021, Proceedings 18*, pages 409–424. Springer, 2021.
- [18] Yihong Dong, Ying Peng, Muqiao Yang, Songtao Lu, and Qingjiang Shi. Signal transformer: Complex-valued attention and meta-learning for signal recognition. *arXiv preprint arXiv:2106.04392*, 2021.
- [19] Vladimir Fanaskov and Ivan Oseledets. Spectral neural operators. *arXiv preprint arXiv:2205.10573*, 2022.
- [20] Zunwei Fu, Xianming Hou, and Qingyan Wu. Convergence of fractional fourier series on the torus and applications. *arXiv preprint arXiv:2210.14720*, 2022.

- [21] George M Georgiou and Cris Koutsougeras. Complex domain backpropagation. *IEEE transactions on Circuits and systems II: analog and digital signal processing*, 39(5):330–334, 1992.
- [22] Paul Geuchen and Felix Voigtlaender. Optimal approximation using complex-valued neural networks. *Advances in Neural Information Processing Systems*, 36, 2024.
- [23] Paul Geuchen, Thomas Jahn, and Hannes Matt. Universal approximation with complex-valued deep narrow neural networks. *arXiv preprint arXiv:2305.16910*, 2023.
- [24] Alejandro Gómez-Echavarría, Juan P Ugarte, and Catalina Tobón. The fractional fourier transform as a biomedical signal and image processing tool: A review. *Biocybernetics and Biomedical Engineering*, 40(3):1081–1093, 2020.
- [25] Steven Guan, Ko-Tsung Hsu, and Parag V Chitnis. Fourier neural operator networks: A fast and general solver for the photoacoustic wave equation. *arXiv preprint arXiv:2108.09374*, 2021.
- [26] Gaurav Gupta, Xiongye Xiao, and Paul Bogdan. Multiwavelet-based operator learning for differential equations. *Advances in neural information processing systems*, 34:24048–24062, 2021.
- [27] Zhongkai Hao, Zhengyi Wang, Hang Su, Chengyang Ying, Yinpeng Dong, Songming Liu, Ze Cheng, Jian Song, and Jun Zhu. Gnot: A general neural operator transformer for operator learning. In *International Conference on Machine Learning*, pages 12556–12569. PMLR, 2023.
- [28] Kaiming He, Xiangyu Zhang, Shaoqing Ren, and Jian Sun. Deep residual learning for image recognition. In *Proceedings of the IEEE conference on computer vision and pattern recognition*, pages 770–778, 2016.
- [29] Dan Hendrycks and Kevin Gimpel. Gaussian error linear units (gelus). *arXiv preprint arXiv:1606.08415*, 2016.
- [30] Akira Hirose. *Complex-valued neural networks: theories and applications*, volume 5. World Scientific, 2003.
- [31] Akira Hirose and Shotaro Yoshida. Generalization characteristics of complex-valued feedforward neural networks in relation to signal coherence. *IEEE Transactions on Neural Networks and learning systems*, 23(4):541–551, 2012.
- [32] Tero Karras, Miika Aittala, Samuli Laine, Erik Härkönen, Janne Hellsten, Jaakko Lehtinen, and Timo Aila. Alias-free generative adversarial networks. *Advances in neural information processing systems*, 34: 852–863, 2021.
- [33] Taehwan Kim and Tülay Adalı. Approximation by fully complex multilayer perceptrons. *Neural computation*, 15(7):1641–1666, 2003.
- [34] Diederik P Kingma and Jimmy Ba. Adam: A method for stochastic optimization. *arXiv preprint arXiv:1412.6980*, 2014.
- [35] Manny Ko, Ujjawal K Panchal, Héctor Andrade-Loarca, and Andres Mendez-Vazquez. Coshnet: A hybrid complex valued neural network using shearlets. *arXiv preprint arXiv:2208.06882*, 2022.
- [36] Nikola Kovachki, Samuel Lanthaler, and Siddhartha Mishra. On universal approximation and error bounds for fourier neural operators. *Journal of Machine Learning Research*, 22(290):1–76, 2021.
- [37] Nikola Kovachki, Zongyi Li, Burigede Liu, Kamyar Azizzadenesheli, Kaushik Bhattacharya, Andrew Stuart, and Anima Anandkumar. Neural operator: Learning maps between function spaces. *arXiv preprint arXiv:2108.08481*, 2021.
- [38] Thorsten Kurth, Shashank Subramanian, Peter Harrington, Jaideep Pathak, Morteza Mardani, David Hall, Andrea Miele, Karthik Kashinath, and Anima Anandkumar. Fourcastnet: Accelerating global high-resolution weather forecasting using adaptive fourier neural operators. In *Proceedings of the Platform for Advanced Scientific Computing Conference*, pages 1–11, 2023.
- [39] ChiYan Lee, Hideyuki Hasegawa, and Shangce Gao. Complex-valued neural networks: A comprehensive survey. *IEEE/CAA Journal of Automatica Sinica*, 9(8):1406–1426, 2022.
- [40] Changpin Li and An Chen. Numerical methods for fractional partial differential equations. *International Journal of Computer Mathematics*, 95(6-7):1048–1099, 2018.
- [41] Yong Li, Zhiqun Song, and Xuejun Sha. The multi-weighted type fractional fourier transform scheme and its application over wireless communications. *EURASIP Journal on wireless communications and networking*, 2018(1):1–10, 2018.

- [42] Zhijie Li, Wenhui Peng, Zelong Yuan, and Jianchun Wang. Long-term predictions of turbulence by implicit u-net enhanced fourier neural operator. *Physics of Fluids*, 35(7), 2023.
- [43] Zongyi Li, Nikola Kovachki, Kamyar Azizzadenesheli, Burigede Liu, Kaushik Bhattacharya, Andrew Stuart, and Anima Anandkumar. Fourier neural operator for parametric partial differential equations. *arXiv preprint arXiv:2010.08895*, 2020.
- [44] Zongyi Li, Daniel Zhengyu Huang, Burigede Liu, and Anima Anandkumar. Fourier neural operator with learned deformations for pdes on general geometries. *arXiv preprint arXiv:2207.05209*, 2022.
- [45] Xinliang Liu, Bo Xu, and Lei Zhang. Ht-net: Hierarchical transformer based operator learning model for multiscale pdes. *arXiv preprint arXiv:2210.10890*, 2022.
- [46] Ze Liu, Yutong Lin, Yue Cao, Han Hu, Yixuan Wei, Zheng Zhang, Stephen Lin, and Baining Guo. Swin transformer: Hierarchical vision transformer using shifted windows. In *Proceedings of the IEEE/CVF international conference on computer vision*, pages 10012–10022, 2021.
- [47] Lu Lu, Pengzhan Jin, Guofei Pang, Zhongqiang Zhang, and George Em Karniadakis. Learning nonlinear operators via deepnet based on the universal approximation theorem of operators. *Nature machine intelligence*, 3(3):218–229, 2021.
- [48] AC McBride and FH Kerr. On namias’s fractional fourier transforms. *IMA Journal of applied mathematics*, 39(2):159–175, 1987.
- [49] R Naveen Kumar, BN Jagadale, and JS Bhat. A lossless image compression algorithm using wavelets and fractional fourier transform. *SN Applied Sciences*, 1:1–8, 2019.
- [50] Tohru Nitta. On the critical points of the complex-valued neural network. In *Proceedings of the 9th International Conference on Neural Information Processing, 2002. ICONIP’02.*, volume 3, pages 1099–1103. IEEE, 2002.
- [51] Tohru Nitta. Orthogonality of decision boundaries in complex-valued neural networks. *Neural computation*, 16(1):73–97, 2004.
- [52] Alan V Oppenheim and Jae S Lim. The importance of phase in signals. *Proceedings of the IEEE*, 69(5): 529–541, 1981.
- [53] Haldun M Ozaktas and M Alper Kutay. The fractional fourier transform. In *2001 European Control Conference (ECC)*, pages 1477–1483. IEEE, 2001.
- [54] Md Ashiqur Rahman, Zachary E Ross, and Kamyar Azizzadenesheli. U-no: U-shaped neural operators. *arXiv preprint arXiv:2204.11127*, 2022.
- [55] Bogdan Raonic, Roberto Molinaro, Tim De Ryck, Tobias Rohner, Francesca Bartolucci, Rima Alaifari, Siddhartha Mishra, and Emmanuel de Bézenac. Convolutional neural operators for robust and accurate learning of pdes. *Advances in Neural Information Processing Systems*, 36, 2024.
- [56] Shubhankar Rawat, KPS Rana, and Vineet Kumar. A novel complex-valued convolutional neural network for medical image denoising. *Biomedical Signal Processing and Control*, 69:102859, 2021.
- [57] David P Reichert and Thomas Serre. Neuronal synchrony in complex-valued deep networks. *arXiv preprint arXiv:1312.6115*, 2013.
- [58] Olaf Ronneberger, Philipp Fischer, and Thomas Brox. U-net: Convolutional networks for biomedical image segmentation. In *Medical Image Computing and Computer-Assisted Intervention—MICCAI 2015: 18th International Conference, Munich, Germany, October 5-9, 2015, Proceedings, Part III 18*, pages 234–241. Springer, 2015.
- [59] Granville Sewell. *Analysis of a finite element method: PDE/PROTRAN*. Springer Science & Business Media, 2012.
- [60] Muhammad Shabbir. *Approximation of chirp functions by fractional Fourier series*. PhD thesis, Dissertation, Lübeck, Universität zu Lübeck, 2019, 2019.
- [61] Alasdair Tran, Alexander Mathews, Lexing Xie, and Cheng Soon Ong. Factorized fourier neural operators. *arXiv preprint arXiv:2111.13802*, 2021.
- [62] Tapas Tripura and Souvik Chakraborty. Wavelet neural operator: a neural operator for parametric partial differential equations. *arXiv preprint arXiv:2205.02191*, 2022.

- 514 [63] Théo Trouillon and Maximilian Nickel. Complex and holographic embeddings of knowledge graphs: a
515 comparison. *arXiv preprint arXiv:1707.01475*, 2017.
- 516 [64] Mark Tygert, Joan Bruna, Soumith Chintala, Yann LeCun, Serkan Piantino, and Arthur Szlam. A
517 mathematical motivation for complex-valued convolutional networks. *Neural computation*, 28(5):815–825,
518 2016.
- 519 [65] Michael Unser. Sampling-50 years after shannon. *Proceedings of the IEEE*, 88(4):569–587, 2000.
- 520 [66] M Vetterli, J Kovacevic, and VK Goyal. Foundations of signal processing, cambridge university press,
521 cambridge, 2014, 2014.
- 522 [67] Felix Voigtlaender. The universal approximation theorem for complex-valued neural networks. *Applied
523 and Computational Harmonic Analysis*, 64:33–61, 2023.
- 524 [68] Rui Wang, Karthik Kashinath, Mustafa Mustafa, Adrian Albert, and Rose Yu. Towards physics-informed
525 deep learning for turbulent flow prediction. In *Proceedings of the 26th ACM SIGKDD International
526 Conference on Knowledge Discovery & Data Mining*, pages 1457–1466, 2020.
- 527 [69] Gege Wen, Zongyi Li, Kamyar Azizzadenesheli, Anima Anandkumar, and Sally M Benson. U-fno—an
528 enhanced fourier neural operator-based deep-learning model for multiphase flow. *Advances in Water
529 Resources*, 163:104180, 2022.
- 530 [70] Scott Wisdom, Thomas Powers, John Hershey, Jonathan Le Roux, and Les Atlas. Full-capacity unitary
531 recurrent neural networks. *Advances in neural information processing systems*, 29, 2016.
- 532 [71] Daniel E Worrall, Stephan J Garbin, Daniyar Turmukhambetov, and Gabriel J Brostow. Harmonic networks:
533 Deep translation and rotation equivariance. In *Proceedings of the IEEE conference on computer vision and
534 pattern recognition*, pages 5028–5037, 2017.
- 535 [72] Haixu Wu, Tengge Hu, Huakun Luo, Jianmin Wang, and Mingsheng Long. Solving high-dimensional pdes
536 with latent spectral models. *arXiv preprint arXiv:2301.12664*, 2023.
- 537 [73] Wei Xiong, Xiaomeng Huang, Ziyang Zhang, Ruixuan Deng, Pei Sun, and Yang Tian. Koopman neural
538 operator as a mesh-free solver of non-linear partial differential equations. *arXiv preprint arXiv:2301.10022*,
539 2023.
- 540 [74] Muqiao Yang, Martin Q Ma, Dongyu Li, Yao-Hung Hubert Tsai, and Ruslan Salakhutdinov. Complex
541 transformer: A framework for modeling complex-valued sequence. In *ICASSP 2020-2020 IEEE Inter-
542 national Conference on Acoustics, Speech and Signal Processing (ICASSP)*, pages 4232–4236. IEEE,
543 2020.
- 544 [75] Hu Yu, Jie Huang, Lingzhi Li, Feng Zhao, et al. Deep fractional fourier transform. *Advances in Neural
545 Information Processing Systems*, 36, 2024.
- 546 [76] Hongkai Zheng, Weili Nie, Arash Vahdat, Kamyar Azizzadenesheli, and Anima Anandkumar. Fast
547 sampling of diffusion models via operator learning. In *International Conference on Machine Learning*,
548 pages 42390–42402. PMLR, 2023.

Appendix

A Fractional Fourier Transform

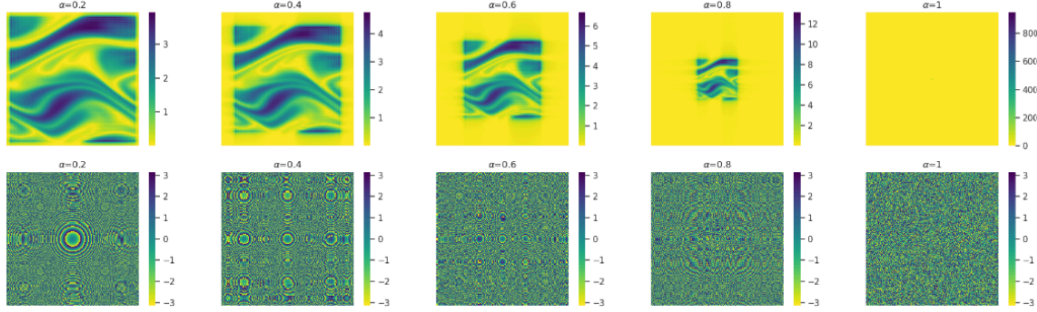


Figure 6: The figure illustrates the FrFT of the Navier-Stokes Partial Differential Equation (PDE) across varying α values. The **(Top)** displays heatmaps representing the magnitude of the transformed data, while the **(Bottom)** showcases corresponding heatmaps depicting the phase angle. Each column corresponds to a distinct α value, highlighting the impact of fractional Fourier transform parameters on the learned representation of the Navier-Stokes PDE. It is observed that in FT, most spectrum is concentrated at low frequency for $\alpha = 1$.

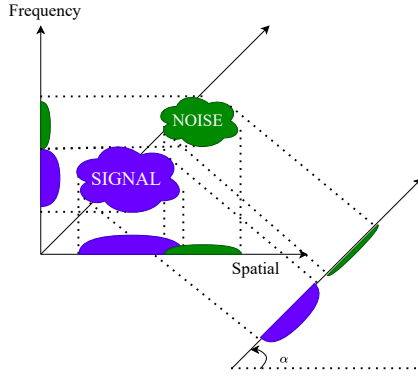


Figure 7: The figure illustrates the inherent optimality of FrFT in signal filtering for non-stationary image signals, showcasing its ability to separate effects along the fractional order axis and examining its relationship with spatial-frequency plane rotation.

in handling non-stationary image signals. It offers valuable insights into its utility and potential applications in the broader signal-processing domain. Fig. 6 shows that as the parameter α increases, the spectral distribution becomes increasingly concentrated around the origin. This concentration results in a loss of spatial information while emphasizing frequency information. Conversely, lower values of α reveal the preservation of information in the phase domain, which, unfortunately, becomes increasingly noisy when transformed into the frequency domain. This behavior highlights the delicate balance between spatial and frequency information, emphasizing the parameter α 's critical role in shaping the signal's characteristics.

B Mathematical Analysis

In this section, we will first present the necessary definitions and then prove the theorem as stated in the main content of the paper. Subsequently, we present a theoretical analysis of several components of the proposed method.

Definition B.1 (Fractional Torus). [20] Let consider $\alpha \in \mathbb{R}$, and $\alpha \neq n\mathbb{Z}$. Define fractional torus of order α , denoted as \mathcal{T}_α^n is the cube $[0, |\sin \alpha|]^n$ with opposite sides identified. We will define FrFT on \mathcal{T}_α^n for the rest of the analysis. We will define Fractional convolution and fractional approximation in $L^p(\mathcal{T}_\alpha^n)$ for $1 \leq p \leq \infty$.

588 **Definition B.2.** Let $\alpha \in \mathcal{R}$ and $\alpha \neq n$. Define $e_\alpha(x) = e^{i\pi|x|^2 \cot \alpha}$ and $e_\alpha f(x) = e_\alpha(x)f(x)$ for function on
589 \mathcal{T}_α^n .

590 **Definition B.3.** Let $1 \leq p \leq \infty$. A function f on \mathcal{T}_α^n lies in the space $e_{-\alpha}L^p(\mathcal{T}_\alpha^n)$ if

$$f(x) = e_{-\alpha}g(x), \quad g \in L^p(\mathcal{T}_\alpha^n) \quad (12)$$

591 and $\|f\|_{L^p(\mathcal{T}_\alpha^n)} < \infty$.

592 **Definition B.4** (Fractional Fourier Transform on Fractional Torus Fu et al. [20]). For complex-valued functions
593 $f \in e_{-\alpha}L^1(\mathcal{T}_\alpha^n)$, $\alpha \in \mathbb{R}$ and $m \in \mathbb{Z}^n$, we define,

$$\mathcal{F}^\alpha(f)(m) = \begin{cases} \int_{\mathcal{T}_\alpha^n} f(x) K_\alpha(m, x) dx & \alpha \neq \pi(Z) \\ f(m) & \alpha = 2\pi(Z) \\ f(-m) & \alpha = 2\pi(Z) + \pi \end{cases} \quad (13)$$

594 where,

$$K_\alpha(m, x) = A_\alpha^n e_\alpha(x) e_\alpha(m, x) e_\alpha(m) \quad (14)$$

595 here, $A_\alpha = \sqrt{1 - i \cot \alpha}$ and $e_\alpha(m, x) = e^{-i2\pi(m \cdot x) \csc \alpha}$. where $\mathcal{F}^\alpha(f)(m)$ denotes the m^{th} fractional
596 fourier coefficient of order α for $f \in e_{-\alpha}L^1(\mathcal{T}_\alpha^n)$.

597 **Remark B.5.** For Eq. 13, it reduces to **Fourier Transform (FT)** when $\alpha = \frac{\pi}{2}$, $\cot \alpha = 0$ and $\csc \alpha = 1$, where

$$K_\alpha(m, x) = e^{-i2\pi(m \cdot x)} \quad (15)$$

598 **Proposition B.6** (Linear and Bounded Operator). Let f, g be in $e_{-\alpha}L^1(\mathcal{T}_\alpha^n)$. Then for $m, k \in \mathbb{Z}^n$, $\lambda \in \mathbb{C}$,
599 $y \in \mathcal{T}_\alpha^n$ then following holds true.

- 600 1. $\mathcal{F}^\alpha(f + g)(m) = \mathcal{F}^\alpha(f)(m) + \mathcal{F}^\alpha(g)(m)$.
- 601 2. $\mathcal{F}^\alpha(\lambda f)(m) = \lambda \mathcal{F}^\alpha(f)(m)$.
- 602 3. $\sup_{m \in \mathbb{Z}^n} |\mathcal{F}^\alpha(f)(m)| \leq |\csc \alpha|^{\frac{n}{2}} \|f\|_{L^1(\mathcal{T}_\alpha^n)}$

603 **Proof:** For proof refer Fu et al. [20].

604 **Proposition B.7** (Uniqueness of Fractional Fourier Transform). If $f, g \in e_{-\alpha}L^1(\mathcal{T}_\alpha^n)$ satisfy $\mathcal{F}^\alpha(f)(m) =$
605 $\mathcal{F}^\alpha(g)(m)$ for all $m \in \mathbb{Z}^n$, then $f = g$ a.e.

606 **Proof:** For proof refer Fu et al. [20].

607 **Corollary B.8** (Fractional Fourier Inversion). If $f \in e_{-\alpha}L^1(\mathcal{T}_\alpha^n)$ and

$$\sum_{m \in \mathbb{Z}^n} |\mathcal{F}^\alpha(f)(m)| < \infty. \quad (16)$$

608 Then,

$$f(x) = \sum_{m \in \mathbb{Z}^n} \mathcal{F}^\alpha(f)(m) K_{-\alpha}(m, x) \text{ a.e.} \quad (17)$$

609 and therefore, f is almost everywhere, equal to a continuous function.

610 **Theorem B.9 (Product Rule).** Suppose $\mathcal{K}_\alpha(m_1, x_1, m_2, x_2, \dots, m_n, x_n)$ denote the fractional integral kernel
611 of the N -dimensional FrFT of a signal $f(x_1, x_2, \dots, x_n)$ with m_1, m_2, \dots, m_n denoting the multidimensional FrFT
612 coefficients, then the following fractional kernel property holds:

$$\mathcal{K}_\alpha(m_1, x_1, m_2, x_2, \dots, m_n, x_n) = \prod_{i=1}^N \mathcal{K}_\alpha(m_i, x_i) \quad (18)$$

613 **Proof:**

614 Let consider the N -dimensional signal $f(x_1, x_2, \dots, x_n)$,

615 Then, let's define the FrFT of the signal as follows:

$$\mathcal{F}^\alpha(f)(m_1, m_2, \dots, m_N) = \int_{-\infty}^{\infty} \dots \int_{-\infty}^{\infty} f(x_1, x_2, \dots, x_N) \prod_{i=1}^N \mathcal{K}_\alpha(m_i, x_i) dx_i, \quad (19)$$

616 From Eq. 19, we can easily prove for $\alpha = 0$,

$$\mathcal{F}^\alpha(f)(m_1, m_2, \dots, m_N) = f(x_1, x_2, \dots, x_n) \quad (20)$$

617 and for $\alpha = 1$, it reduces to *Fourier Transform (FT)*.

618 Therefore, if we can show that $\mathcal{F}^\alpha \mathcal{F}^\beta = \mathcal{F}^{\alpha+\beta}$ then obviously \mathcal{F}^α satisfy all the FrFT properties.

619 Then,

$$\mathcal{F}^\alpha \mathcal{F}^\beta(f)(m_1, m_2, \dots, m_n) = \int_{-\infty}^{\infty} \dots \int_{-\infty}^{\infty} \prod_{i=1}^N \mathcal{K}_\alpha(m_i, x_i) \int_{-\infty}^{\infty} \dots \int_{-\infty}^{\infty} f(y_1, y_2, \dots, y_N) \prod_{i=1}^N \mathcal{K}_\beta(x_i, y_i) dy_i dx_i \quad (21)$$

$$\mathcal{F}^\alpha \mathcal{F}^\beta(f)(m_1, m_2, \dots, m_n) = \int_{-\infty}^{\infty} \dots \int_{-\infty}^{\infty} f(y_1, y_2, \dots, y_N) \left\{ \prod_{i=1}^N \int_{-\infty}^{\infty} \mathcal{K}_\alpha(m_i, x_i) \mathcal{K}_\beta(x_i, y_i) dx_i \right\} dy_1 dy_2 \dots dy_n \quad (22)$$

620 Now using the result from [2],

$$\int_{-\infty}^{\infty} \mathcal{K}_\alpha(m, x) \mathcal{K}_\beta(x, y) dx = \mathcal{K}_{\alpha+\beta}(m, y) \quad (23)$$

621 Using the above property,

$$\mathcal{F}^\alpha \mathcal{F}^\beta(f)(m_1, m_2, \dots, m_n) = \int_{-\infty}^{\infty} \dots \int_{-\infty}^{\infty} f(y_1, y_2, \dots, y_N) \prod_{i=1}^N \mathcal{K}_{\alpha+\beta}(m_i, y_i) dy_1 dy_2 \dots dy_n = \mathcal{F}^{\alpha+\beta} \quad (24)$$

622 Therefore, we conclude that,

$$\mathcal{K}_\alpha(m_1, x_1, m_2, x_2, \dots, m_n, x_n) = \prod_{i=1}^N \mathcal{K}_\alpha(m_i, x_i) \quad (25)$$

623 **Definition B.10.** Let f and g be square integrable functions, Let, $h(x) = (f * g)(x)$ (where $*$ denotes the
624 convolution), i.e.,

$$h(x) = (f * g)(x) = \int_{-\infty}^{\infty} f(t)g(x-t) dt. \quad (26)$$

625 **Definition B.11.** For any function $f(x)$, let us define the function $e_\alpha f(x) = e_\alpha(x)f(x)$. For any two functions
626 f and g , we define the convolution operation $*$ by

$$h(x) = (f * g)(x) = A_\alpha e_{-\alpha}(x)(e_\alpha f * e_\alpha g)(x), \quad (27)$$

627 where $*$ is the convolution operation as defined in Eq. 26.

628 **Theorem B.12 (Convolution Theorem for Fractional Fourier Transform (FrFT)).** Suppose f and g are
629 square-integrable functions. Define $e_\alpha(m) = e^{i\pi|m|^2 \cot(\alpha)}$ and $h(x) = (f * g)(x)$ where $*$ denotes the usual
630 convolution integral with \mathcal{F}^α , \mathcal{G}^α , \mathcal{H}^α respectively denoting the FrFT of f , g and h , respectively. Then,

$$\mathcal{H}^\alpha(m) = \mathcal{F}^\alpha(m)\mathcal{G}^\alpha(m)e_{-\alpha}(m). \quad (28)$$

631 **Proof:** By FrFT definition from Eq. 2, we know that

$$\begin{aligned} \mathcal{H}^\alpha(h)(m) &= A_\alpha \int_{-\infty}^{\infty} h(t) e_\alpha(t) e_\alpha(m, t) e_\alpha(m) dt \\ &= A_\alpha^2 \int_{-\infty}^{\infty} e_\alpha(t) e_\alpha(m, t) e_\alpha(m) e_{-\alpha}(t) dt \int_{-\infty}^{\infty} e_\alpha(x) f(x) e_\alpha(t-x) g(t-x) dx \\ &= A_\alpha^2 \int_{-\infty}^{\infty} \int_{-\infty}^{\infty} f(x) g(t-x) e_\alpha(t) e_\alpha(m, t) e_\alpha(m) e_{-\alpha}(t) e_\alpha(x) e_\alpha(t-x) dx dt \end{aligned} \quad (29)$$

632 By substituting $t-x = v$ in the above eq. , we obtain

$$\begin{aligned}
\mathcal{H}^\alpha(h)(m) &= A_\alpha^2 e_\alpha(m) \int_{-\infty}^{\infty} \int_{-\infty}^{\infty} f(x)g(v)e_\alpha(x+v)e_\alpha(m, x+v)e_{-\alpha}(x+v)e_\alpha(x)e_\alpha(v)dx dv \\
&= A_\alpha^2 e_{-\alpha}(m) \int_{-\infty}^{\infty} f(x)e_\alpha(x)e_\alpha(m)e_\alpha(m, x)dx \int_{-\infty}^{\infty} g(v)e_\alpha(v)e_\alpha(m)e_\alpha(m, v)dv \\
&= \mathcal{F}^\alpha(m)\mathcal{G}^\alpha(m)e_{-\alpha}(m)
\end{aligned} \tag{30}$$

Therefore, we have,

$$\mathcal{H}^\alpha(m) = \mathcal{F}^\alpha(m)\mathcal{G}^\alpha(m)e_{-\alpha}(m). \tag{31}$$

Definition B.13 (Fractional Fourier Projection Operator). Let's define the Fractional Fourier wave-number as follows:

$$\mathcal{K}_N = \{k \in \mathbb{Z}^n : |k|_\infty \leq N\} \tag{32}$$

And define fractional projection operator to truncate high order coefficient of a function as follows:

$$\mathcal{P}_N(f)(x) = \mathcal{F}^{-\alpha}(\mathcal{F}^\alpha(f)(k) \cdot \mathbf{1}_{\mathcal{K}_N}(k)) \tag{33}$$

where $\mathbf{1}_{\mathcal{K}_N}(k)$ indicates indicator function which takes 1 when $k \in \mathcal{K}_N$ and 0 otherwise.

Theorem B.14 (Convergence of Fractional Fourier Series). Let $\alpha \in \mathbb{R}$ and $\alpha \neq \pi\mathbb{Z}$, and $f \in e_{-\alpha}L^p(\mathcal{T}_\alpha^n)$ ($1 \leq p < \infty$), $\mathcal{P}_N(f)(x)$ denotes as follows:

$$\mathcal{P}_N(f)(x) = \mathcal{F}^{-\alpha}(\mathcal{F}^\alpha(f)(k) \cdot \mathbf{1}_{\mathcal{K}_N}(k)) \tag{34}$$

where, $\mathcal{F}^\alpha(f)(k)$ denotes the k^{th} fractional coefficient. Then,

$$\lim_{N \rightarrow \infty} \sup_x ||f(x) - \mathcal{P}_N(f)(x)|| \rightarrow 0 \tag{35}$$

Theorem B.15 (Universal Approximation of CoNO). Let $s, s' > 0$ and $\alpha \in \mathbb{R}$; Suppose $\mathcal{G} : H^s(\mathcal{T}_\alpha^d; \mathbb{R}^{d_u}) \rightarrow H^{s'}(\mathcal{T}_\alpha^d; \mathbb{R}^{d_u})$ represent a continuous operator between Sobolev spaces where \mathcal{T}_α^d denotes the fractional order torus and $d_\alpha, d_u \in \mathbb{N}$; and $K \subset H^s(\mathcal{T}_\alpha^d; \mathbb{R}^{d_{in}})$ is a compact subset. Then, for any $\varepsilon > 0$, there exists CoNO layers $\mathcal{N} : H^s(\mathcal{T}_\alpha^d; \mathbb{R}^{d_{in}}) \rightarrow H^{s'}(\mathcal{T}_\alpha^d; \mathbb{R}^{d_{out}})$ satisfying:

$$\sup_{v \in K} ||\mathcal{G}(v) - \mathcal{N}(v)||_{L^2} \leq \varepsilon \tag{36}$$

Proof: Let $\alpha \in \mathbb{R}$ and define the following fractional orthogonal projection operator:

$$\mathcal{G}_N : H^s(\mathcal{T}_\alpha^d) \rightarrow H^{s'}(\mathcal{T}_\alpha^d), \quad \mathcal{G}_N(v) = \mathcal{P}_N \mathcal{G}(\mathcal{P}_N(v)) \tag{37}$$

Using Thm. B.14, we have for $\forall \varepsilon$, there exists $N \geq 0$ such that:

$$||\mathcal{G}(v) - \mathcal{G}_N(v)||_{L^2} \leq \varepsilon, \quad \forall v \in K \tag{38}$$

We need to find \mathcal{N} to approximate \mathcal{G}_N .

Next we define *Fractional Conjugate* of \mathcal{G}_N as follows:

$$\hat{\mathcal{G}}_N : \mathbb{C}^{\mathcal{K}_N} \rightarrow \mathbb{C}^{\mathcal{K}_N}, \quad \hat{\mathcal{G}}_N(\hat{v}) = \mathcal{F}^\alpha(\mathcal{G}_N(\mathcal{F}^{-\alpha}(\hat{v}))) \tag{39}$$

we can show that,

$$\mathcal{G}_N = \mathcal{F}^{-\alpha} \circ \hat{\mathcal{G}}_N \circ (\mathcal{F}^\alpha \circ \mathcal{P}_N) \tag{40}$$

Now with above decomposition, we can construct CoNO by separately approximating each individual terms $\mathcal{F}^{-\alpha}$, $\hat{\mathcal{G}}_N$ and $\mathcal{F}^\alpha \circ \mathcal{P}_N$.

Approximating $\hat{\mathcal{G}}_N$: For $\forall \varepsilon \geq 0$ and $\hat{\mathcal{G}}_N : \mathbb{C}^{\mathcal{K}_N} \rightarrow \mathbb{C}^{\mathcal{K}_N}$, we have l CoNO layers $\mathcal{L}_l \circ \mathcal{L}_{l-1} \circ \dots \circ \mathcal{L}_1$ which satisfy:

$$||\hat{\mathcal{G}}_N(\hat{v})(x) - (\mathcal{L}_l \circ \mathcal{L}_{l-1} \circ \dots \circ \mathcal{L}_1)(\hat{w})(x)||_{L^2} \leq \varepsilon, \quad \forall v \in K, \forall x \in \mathcal{T}_\alpha^d \tag{41}$$

where, $\hat{w} : \mathcal{T}_\alpha^d, x \rightarrow \hat{v}$ is constant function defined on \mathcal{T}_α^d .

From CoNO layer definition, we have,

$$\mathcal{L}_l(v)(x) = Wv(x) + \mathcal{F}^{-\alpha}(K_l(k)\mathcal{F}^\alpha(\mathcal{P}_N v)(k)) \tag{42}$$

656 To approximate $\hat{\mathcal{G}}_N$, we can use *Universal Approximation Theorem for CVNNs* [67] by setting $K_l(k)$ to be
 657 identity. Then,

$$\mathcal{F}^{-\alpha}(K_l(k)\mathcal{F}^\alpha(\mathcal{P}_N v)(k)) \approx \mathcal{P}_N(v), \quad \forall l, \quad (43)$$

658 then we have,

$$\mathcal{L}_l(v)(x) = Wv(x) + \mathcal{P}_N(v)(x) \quad (44)$$

659 And then using the Universal Approximation Theorem for CVNNs will guarantee that $\mathcal{L}_l \circ \mathcal{L}_{l-1} \circ \dots \circ \mathcal{L}_1$ can
 660 approximate $\hat{\mathcal{G}}_N$ to any desired precision.

661 **Approximating** $\mathcal{F}^\alpha \circ \mathcal{P}_N$: For any $\varepsilon \geq 0$ there exists $l \geq 0$ and $\mathcal{L}_l \circ \mathcal{L}_{l-1} \circ \dots \circ \mathcal{L}_1 \circ \mathcal{P}$ that satisfy following:

$$\|\mathcal{F}^\alpha(\mathcal{P}_N v) - (\mathcal{L}_l \circ \mathcal{L}_{l-1} \circ \dots \circ \mathcal{L}_1 \circ \mathcal{P})(v)(x)\|_{L^2} \leq \varepsilon, \quad \forall v \in K, \forall x \in \mathcal{T}^d \quad (45)$$

662 Let's define $\mathcal{R}(k, x) = e_\alpha(k)e_\alpha(k, x)$ which constitutes the orthonormal basis for FrFT, which we call as
 663 fractional fourier basis.

664 Firstly we will show that there exists $\mathcal{N} = \mathcal{L}_l \circ \mathcal{L}_{l-1} \circ \dots \circ \mathcal{L}_1 \circ \mathcal{P}$ that satisfies:

$$\begin{cases} \|\mathcal{N}(v)_{1,k} - \mathcal{P}_N v(x).Re(\mathcal{R}(k, x))\|_{L^2} < \varepsilon \\ \|\mathcal{N}(v)_{1,k} - \mathcal{P}_N v(x).Im(\mathcal{R}(k, x))\|_{L^2} < \varepsilon \end{cases} \quad (46)$$

665 To construct \mathcal{N} , we define the lifting operator \mathcal{P} and use position embedding as follows:

$$\mathcal{P}(v) = R(v(x) = \{v(x), Re(\mathcal{R}(k, x)), v(x), Im(\mathcal{R}(k, x))\}_{k \in \mathcal{K}_N} \quad (47)$$

666 where trigonometric polynomial of order α are directly embedded in CONO layer. \mathcal{P} lifts the range of function
 667 from \mathbb{R}^{d_a} to \mathbb{R}^{d_u} . Then, by leveraging the Universal Approximation Theorem for CVNNs where we concatenate
 668 the $\{v.Re(\mathcal{R}(k, x)), v.Im(\mathcal{R}(k, x))\}_{k \in \mathcal{K}_N}$, we can have multiple layers satisfies:

$$(\mathcal{L}_l \circ \dots \circ \mathcal{L}_1)(\{v(x), Re(\mathcal{R}(k, x)), v(x), Im(\mathcal{R}(k, x))\}_{k \in \mathcal{K}_N}) \approx \{v.Re(\mathcal{R}(k, x)), v.Im(\mathcal{R}(k, x))\}_{k \in \mathcal{K}_N}, \quad \forall v \in K \quad (48)$$

669 And can achieve the desired precision by adjusting the width and depth of the layers. We next note that,

$$\mathcal{P}_N v(x) = \sum_{k \in \mathcal{K}_N} \hat{v}_k K_{-\alpha}(k, x) \quad (49)$$

670 where \hat{v}_k denotes the k^{th} coefficient of FrFT. Then by definition of FrFT in Eq 2:

$$\mathcal{F}^\alpha(v)(0) = \int_{\mathcal{T}_\alpha^d} v(x) A_\alpha e_\alpha(x) dx = Re(\hat{v}_0) + Im(\hat{v}_0) \quad (50)$$

$$\mathcal{F}^\alpha(v.\mathcal{R}(k, x))(0) = \int_{\mathcal{T}_\alpha^d} v(x) A_\alpha e_\alpha(x) e_\alpha(k) e_\alpha(k, x) dx = Re(\hat{v}_k) + Im(\hat{v}_k) \quad (51)$$

671 Thus in layer \mathcal{L}_{l+1} :

$$\begin{cases} K_{l+1}(k) = 0 & \text{if } k = 0 \\ K_{l+1}(k) = -Id & \text{if } k \neq 0 \end{cases} \quad (52)$$

672 And then we have:

$$\mathcal{F}^{-\alpha}(K_{l+1}(k).\mathcal{F}^\alpha(\{v.Re(\mathcal{R}(k, x)), v.Im(\mathcal{R}(k, x))\}_{k \in \mathcal{K}_N})) = \{Re(\hat{v}_k) - v.Re(\mathcal{R}(k, x)), Im(\hat{v}_k) - v.Im(\mathcal{R}(k, x))\}_{k \in \mathcal{K}_N} \quad (53)$$

673 Finally, we can set W_{l+1} in layer \mathcal{L}_{l+1} to be identity we get,

$$\mathcal{L}_{l+1}(\{v.Re(\mathcal{R}(k, x)), v.Im(\mathcal{R}(k, x))\}_{k \in \mathcal{K}_N})) = \{Re(\hat{v}_k), Im(\hat{v}_k)\}_{k \in \mathcal{K}_N} = \mathcal{F}^\alpha(\mathcal{P}_N v) \quad (54)$$

674 Which is the desired approximation.

675 **Approximating** $\mathcal{F}^{-\alpha}$: For any ε , we have $l \geq 0$ and $\mathcal{Q} \circ \mathcal{L}_l \circ \mathcal{L}_{l-1} \circ \dots \circ \mathcal{L}_1$ that satisfies:

$$\|\mathcal{F}^{-\alpha}(\hat{v}) - (\mathcal{Q} \circ \mathcal{L}_l \circ \mathcal{L}_{l-1} \circ \dots \circ \mathcal{L}_1)(v)\|_{L^2} \leq \varepsilon, \quad \forall v \in K \quad (55)$$

where $\hat{v} \in \mathbb{C}^{\mathcal{K}_N}$ is the truncated fractional fourier coefficient.

We can use the previous steps here as well. We can construct $Re(\hat{v}_k) \cdot \mathcal{R}(k, x)$ and $Im(\hat{v}_k) \cdot \mathcal{R}(k, x)$ using $\mathcal{L}_l \circ \mathcal{L}_{l-1} \circ \dots \circ \mathcal{L}_1$. We can construct projection operator \mathcal{Q} to recover the original function.

$$\mathcal{Q}(\{\hat{v}_k \cdot \mathcal{R}(k, x)\}_{k \in \mathcal{K}_N}) = \sum_{k \in \mathcal{K}_N} Re(\hat{v}_k) \cdot \mathcal{R}(k, x) - Im(\hat{v}_k) \cdot \mathcal{R}(k, x) = v(x) \quad (56)$$

Therefore, it completes our proof.

Using the above approximation for \mathcal{G}_N we can approximate the operator to desired precision. Thus establishing the Universal Approximation Theorem for CoNO.

C Details for the Benchmark

C.1 Details for benchmarks tasks

The following sections comprehensively elucidate details for benchmark tasks.

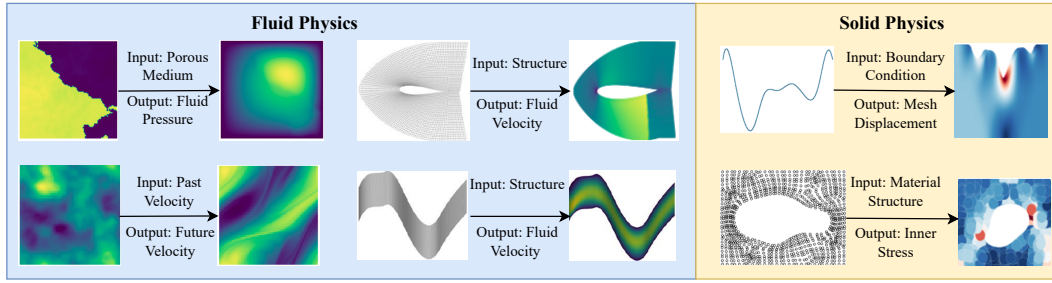


Figure 8: The diagram presents an overview of the Operator learning task applied to distinct Partial Differential Equations (PDEs) classified as Fluid Physics and Solid Physics. **(Top)** showcases three specific PDEs: Darcy Flow, Airfoil, and Plasticity. **(Bottom)**, an additional set of three PDEs is featured: Navier Stokes, Pipe, and Elasticity.

Table 4: Detailed benchmark tasks provide a thorough and systematic exploration of each task’s specific characteristics used in experimentation.

Dataset	Geometry	Task	Input	Output
ELASTICITY-P	Point Cloud	Estimate Stress	Material Structure	Inner Stress
ELASTICITY-G	Regular Grid	Estimate Stress	Material Structure	Inner Stress
PLASTICITY	Structured Mesh	Model Deformation	Boundary Condition	Mesh Displacement
NAVIER-STOKES	Regular Grid	Predict Future	Past Velocity	Future Velocity
AIRFOIL	Structured Mesh	Estimate Velocity	Structure	Fluid Velocity
PIPE	Structured Mesh	Estimate Velocity	Structure	Fluid Velocity
DARCY	Regular Grid	Estimate Pressure	Porous Medium	Fluid Pressure

C.2 Description of Datasets

Table 4 and Fig. 8 comprehensively present the benchmark details. The categorization of generation details is presented according to the governing partial differential equations (PDEs) as follows:

Elasticity-P and Elasticity-G Dataset [44]: The dataset is designed to evaluate internal stress within an incompressible material characterized by an arbitrary void at its center, subject to external tension. The material’s structural configuration constitutes the input, and the resulting internal stress is the output. Notably, two distinct approaches are employed in modeling the material’s geometry: Elasticity-P utilizes a point cloud comprising 972 points. Elasticity-G represents the data on a structured grid with dimensions 41×41 , obtained through interpolation from the Elasticity-P dataset.

Plasticity Dataset [44]: This dataset addresses the plastic forging scenario, wherein a die with an arbitrary shape impacts a plastic material from above. The input to the benchmark is characterized by the die’s shape, encoded in a structured mesh. The benchmark aims to predict the deformation of each mesh point over the subsequent 20 timesteps. The structured mesh employed has a resolution of 101×31 .

698 **Navier Stokes Dataset [43]:** 2D Navier-Stokes equation mathematically describes the flow of a viscous,
699 incompressible fluid in vorticity form on the unit torus as follows:

$$\begin{aligned}\partial_t w(x, t) + u(x, t) \cdot \nabla w(x, t) &= \nu \Delta w(x, t) + f(x), \quad x \in (0, 1)^2, t \in (0, T] \\ \nabla \cdot u(x, t) &= 0, \quad x \in (0, 1)^2, t \in [0, T] \\ w(x, 0) &= w_0(x), \quad x \in (0, 1)^2\end{aligned}\tag{57}$$

700 where, u represents the velocity field, $w = \nabla \times u$ is the vorticity, w_0 is the initial vorticity, ν is the viscosity
701 coefficient, and f is the forcing function. In this dataset, the viscosity (ν) is fixed at 10^{-5} , and the 2D field has a
702 resolution of 64×64 . Each sample within the dataset comprises 20 consecutive frames. The objective is to
703 predict the subsequent ten frames based on the preceding ten.

704 **Pipe Dataset [44]:** This dataset focuses on the incompressible flow through a pipe. The governing equations are
705 Equation 59:

$$\nabla \cdot \mathbf{U} = 0,\tag{58}$$

$$\frac{\partial \mathbf{U}}{\partial t} + \mathbf{U} \cdot \nabla \mathbf{U} = \mathbf{f}^{-1} \frac{1}{\rho} \nabla p + \nu \nabla^2 \mathbf{U}.\tag{59}$$

706 The dataset is constructed on a geometrically structured mesh with a 129×129 resolution. We employ the mesh
707 structure as input data for experimental purposes, with the output being the horizontal fluid velocity within the
708 pipe.

709 **Airfoil Dataset [44]:** The dataset pertains to transonic flow over an airfoil. Due to the negligible viscosity of air,
710 the viscous term $\nu \nabla^2 U$ is omitted from the Navier-Stokes equation. Consequently, the governing equations for
711 this scenario are expressed as follows:

$$\frac{\partial \rho f}{\partial t} + \nabla \cdot (\rho f U) = 0\tag{60}$$

$$\frac{\partial (\rho f U)}{\partial t} + \nabla \cdot (\rho f U U + p I) = 0\tag{61}$$

$$\frac{\partial E}{\partial t} + \nabla \cdot ((E + p)U) = 0,\tag{62}$$

712 where ρf represents fluid density, and E denotes total energy. The data is on a structured mesh with dimensions
713 200×50 , and the mesh point coordinates are utilized as inputs. The corresponding output is the Mach number
714 at each mesh point.

715 **Darcy Flow Dataset [43]:** It represents the flow through porous media. 2D Darcy flow over a unit square is
716 given by

$$\nabla \cdot (a(x) \nabla u(x)) = f(x), \quad x \in (0, 1)^2,\tag{63}$$

$$u(x) = 0, \quad x \in \partial(0, 1)^2.\tag{64}$$

717 where $a(x)$ is the viscosity, $f(x)$ is the forcing term, and $u(x)$ is the solution. This dataset employs a constant
718 value of forcing term $F(x) = \beta$. Further, Equation 63 is modified in the form of a temporal evolution as

$$\partial_t u(x, t) - \nabla \cdot (a(x) \nabla u(x, t)) = f(x), \quad x \in (0, 1)^2,\tag{65}$$

719 In this dataset, the input is represented by the parameter a , and the corresponding output is the solution u . The
720 dataset comprises samples organized on a regular grid with a resolution of 85×85 .

721 D Implementation Details

722 The following section provides a comprehensive overview of the training and testing samples, including details
723 about the shapes of input and output tensors.

Table 5: Training details for benchmark datasets. The input-output resolutions are presented in the shape of (temporal, spatial, variate). The symbol "/" indicates dimensions excluded.

Dataset	Training Samples	Testing Samples	Input Tensor	Output Tensor
ELASTICITY-P	1000	200	(/, 972, 2)	(/, 972, 1)
ELASTICITY-G	1000	200	(/, 41 × 41, 1)	(/, 41 × 41, 1)
PLASTICITY	900	80	(/, 101 × 31, 2)	(20, 101 × 31, 4)
NAVIER-STOKES	1000	200	(10, 64 × 64, 1)	(10, 64 × 64, 1)
AIRFOIL	1000	100	(/, 200 × 50, 2)	(/, 200 × 50, 1)
PIPE	1000	200	(/, 129 × 129, 2)	(/, 129 × 129, 1)
DARCY	1000	200	(/, 85 × 85, 1)	(/, 85 × 85, 1)

D.1 Training Details

Table 5 presents a comprehensive overview of the experimental setup, including details regarding the training and testing split and the shapes of the input and output tensors. This information is crucial for understanding the specific configurations employed in our experimentation process. In training CoNO, we need to initialize the fractional orders, which are learned in the same way as other matrices that are part of our network using optimizers such as Adam. Notably, fractional orders can vary across axes, and there is no requirement for uniformity initialization of fractional orders across different axes. Furthermore, we conducted each experiment five times and observed that the standard deviation falls within the ranges of 0.0003 for Darcy, Airfoil, and Pipe datasets, 0.01 for Navier Stokes, 0.002 for Elasticity-P and Elasticity-G, and 0.0002 for Plasticity.

D.2 Discrete Implementation of Fractional Fourier Transform

The discrete implementation of the Fractional Fourier Transform (FrFT) is essential for CoNO. In CoNO, we utilize a matrix multiplication-based discrete FrFT. This approach leverages the spectral expansion of the fractional integral kernel using a complete set of eigenfunctions of the FrFT, which are Hermite-Gaussian functions [10]. We have used the following PyTorch-based discrete implementation of FrFT: Torch FrFT.

D.3 Complex Neural Networks (CVNNs)

Given that all datasets are inherently real-valued, we designed a neural network optimized for real-valued operations within the complex domain. Using Complex-Valued Neural Networks (CVNNs), the network effectively handles complex data components. It converts real-valued data to complex representations through a residual block, as shown in Fig. 9. This architecture allows the neural network to process the real-valued datasets in the complex domain efficiently. Complex-valued backpropagation was implemented using the Wirtinger calculus [3], which generalizes the notion of complex derivatives and trains complex-valued neural networks (generalized complex chain rule for real-valued loss function) [5, 14]. If L is a real-valued loss function and z is a complex variable such that $z = x + iy$ where $x, y \in \mathbb{R}$:

$$\nabla_z L = \frac{\partial L}{\partial z} = \frac{\partial L}{\partial x} + i \frac{\partial L}{\partial y} = \frac{\partial L}{\partial(\text{Re}(z))} + i \frac{\partial L}{\partial(\text{Im}(z))} = (\nabla_{\text{Re}(z)} L + i(\nabla_{\text{Im}(z)} L)) \quad (66)$$

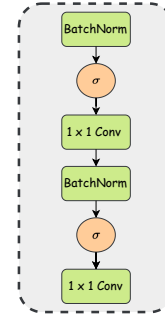


Figure 9: Complex Residual Network used in CoNO for learning the complex part for CVNNs.

Exploring the use of CVNNs with Fourier transforms opens up exciting new possibilities for future research.

We have used Pytorch to build blocks for CoNO based on the following GitHub repositories:

1. Deep Complex Network
2. Pytorch Complex

D.4 Hyperparameters

This section details the hyperparameter values used in CoNO for the different benchmark dataset. For all the benchmarks we have used 4 layers of CoNO. We will specify the settings and configurations, such as learning rates, batch sizes, the number of layers, activation functions, and any other relevant parameters that were

Table 6: Table detailing the hyperparameters used in CoNO for different benchmarks datasets.

Datasets	Learning Rate	Batch Size	Latent Dim	Padding	Gamma	Step-Size
Elasticity-P	0.005	40	64	(7, 7)	0.5	100
Elasticity-G	0.0005	20	64	(0, 0)	0.5	100
Plasticity	0.001	10	64	(12, 1, 11)	0.5	100
Navier Stokes	0.001	20	64	(0, 0)	0.5	100
Darcy	0.001	20	64	(11, 11)	0.5	100
Airfoil	0.001	20	64	(13, 3)	0.5	100
Pipe	0.0005	40	64	(15, 15)	0.5	100

employed to optimize the performance of CoNO on this dataset as shown in Table 6. Further, as shown in Fig. 2 we initialize $\alpha = 1$ and $\alpha' = 0.5$. We further used pointwise convolution in $R^{\alpha'}$ and linear transformation in R^{α} by truncating the higher frequency similar to FNO.

D.5 Mitigation of Aliasing

In Neural Operator learning, the utilization of non-linear operations, such as non-linear pointwise activations, can introduce high-frequency components into the output signal. The manifestation of aliasing induced by nonlinearity can result in distortion of symmetry inherent in the physical signal, leading to undesirable effects. Additionally, the pursuit of translational invariance, a key characteristic in neural operators, becomes susceptible to degradation due to aliasing.

We propose a two-step process to address the challenges of aliasing errors within the continuous equivariance paradigm for CoNO as outline in [32, 55]. Firstly, before applying any activation function, we employ an upsampling operation on the input function, exceeding its frequency bandwidth. Subsequently, a non-linear operation is applied to the upsampled signal, followed by a sinc-based filter and downsampling. Incorporating the sinc-based low-pass filter effectively attenuates higher frequency components in the output signal. This method enhances the accuracy of neural network predictions by minimizing distortions caused by aliasing, which is especially critical in applications dealing with complex signal-processing tasks. Although our experiments did not show significant performance improvement with alias-free activation, we observed a training time slowdown.

E Prediction Visualization

As illustrated in Fig. 10, the performance exhibited by CoNO in predictive tasks surpasses that of other benchmark datasets, notably outperforming the state-of-the-art operator LSM. This superiority is particularly evident in time-dependent and independent partial differential equations (PDEs) scenarios. CoNO showcases enhanced predictive accuracy and significantly reduces artifacts. These compelling findings underscore the efficacy of CoNO as a robust solution for a diverse range of PDE applications, marking a significant advancement in scientific machine learning.

F Experimental Results

The following section provides an exhaustive examination of the results obtained from multiple tasks associated with the operator. These tasks encompass a broad spectrum, including different resolutions, resilience to noise, performance in out-of-generalization tasks, data efficiency, and training stability. The comprehensive analysis presented in this section aims to offer a detailed insight into the performance and capabilities of the operator across a range of critical aspects, contributing to a nuanced understanding of its practical utility and effectiveness in diverse scenarios. All baseline models are instantiated and implemented utilizing the official source code.

F.1 Performance Under Different Resolution

To assess the efficacy of our operator at diverse resolutions, we conducted experiments on Darcy and Navier-Stokes problems across varying spatial resolutions. Notably, CoNO consistently outperformed other operators across these resolutions, demonstrating its superior effectiveness. The comparative results, as presented in Table 7 and Table 8, unequivocally highlight the robust performance and versatility of CoNO in addressing challenges associated with different spatial resolutions in the context of both Darcy and Navier-Stokes scenarios.

The difference in testing errors at different resolutions for the Navier-Stokes experiment can be explained by the inherent nature of the non-linear dynamics involved in turbulent flows. As shown in Table 8 of the main manuscript, the performance of all operators significantly improves with increasing resolution. It is because higher resolutions better capture the complex, high-dimensional dynamics of the flow, which are continuous. The discretized approximation may only partially capture these dynamics at lower resolutions, leading to higher

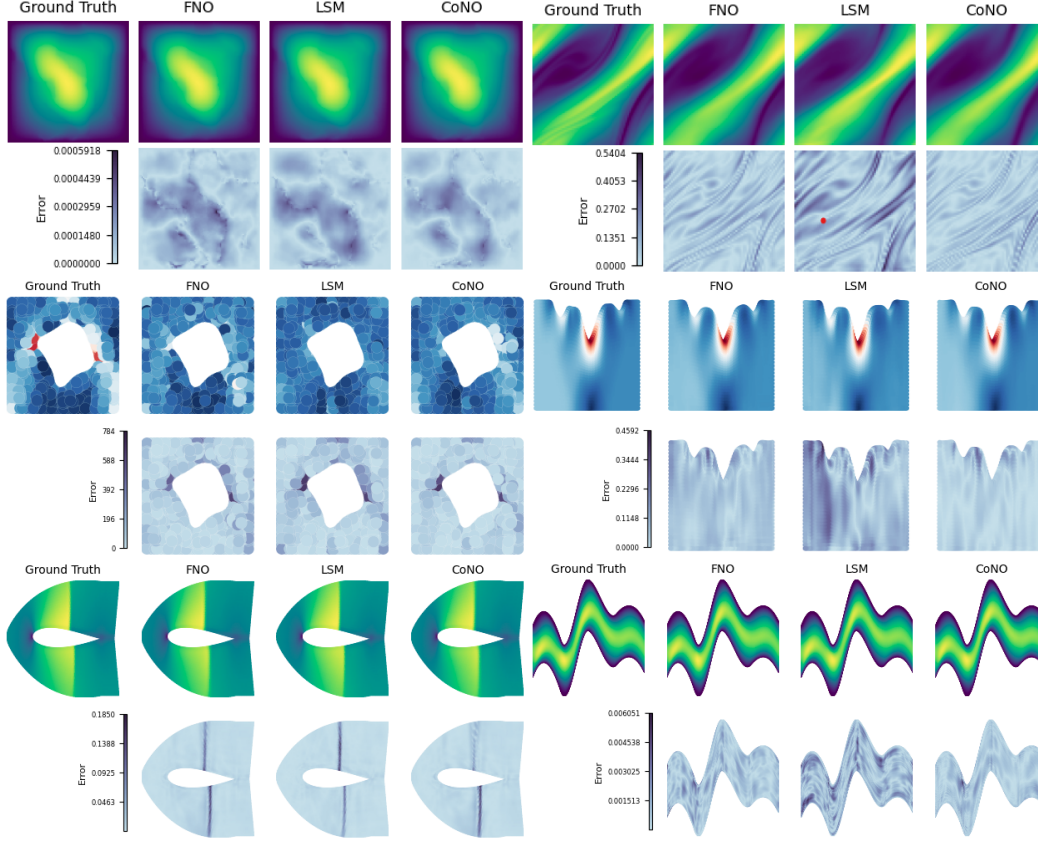


Figure 10: **(Top)** Showcase of Darcy Flow **(Left)** and Navier Stokes **(Right)**. **(Middle)** Showcase of Airfoil **(Right)** and Pipe **(Left)**. **(Bottom)** Showcase of Plasticity **(Left)** and Elasticity **(Right)**. For Comparison of predicted output, we have plotted the heatmap of the absolute value of the difference between Ground Truth and Prediction.

805 errors. As resolution increases, the model can more accurately represent the intricate details of the flow, thereby
806 reducing testing errors. It highlights the importance of resolution in experiments involving the Navier-Stokes
807 equations, where capturing the full dynamics spectrum is crucial for accurate predictions.

Table 7: Neural Operators performance comparison on Darcy Flow under Different Resolutions.

Resolution	UNET	FNO	MWT	UNO	FFNO	HTNET	LSM	CoNO
32x32	0.0059	0.0128	0.0083	0.0148	0.0103	0.0058	0.0049	0.0048
64x64	0.0052	0.0067	0.0078	0.0079	0.0064	0.0046	0.0042	0.0036
128x128	0.0054	0.0057	0.0064	0.0064	0.0050	0.0040	0.0038	0.0034
256x256	0.0251	0.0058	0.0057	0.0064	0.0051	0.0044	0.0043	0.0039
512x512	0.0496	0.0057	0.0066	0.0057	0.0042	0.0063	0.0039	0.0035
1024x1024	0.0754	0.0062	0.0077	0.0058	0.0069	0.0163	0.0050	0.0044

Table 8: Neural Operators performance comparison on the Navier-Stokes Benchmark Under Different Resolutions. "/" indicates poor l_2 error performance.

Resolution	UNET	FNO	MWT	UNO	FFNO	HTNET	LSM	CoNO
64x64	0.1982	0.1556	0.1541	0.1713	0.2322	0.1847	0.1535	0.1287
128x128	/	0.1028	0.1099	0.1068	0.1506	0.1088	0.0961	0.0817

F.2 Robustness to Noise

To evaluate the robustness of our operator in the presence of noisy training input, we systematically conducted experiments across varying input noise levels. Our objective was to comprehensively understand the impact of noise on the performance of the proposed operator. Remarkably, our findings revealed that CoNO, even when subjected to 0.1% data noise, consistently outperformed LSM—the best-performing operator trained without exposure to noisy data. This result is a compelling confirmation of the enhanced robustness exhibited by our proposed operator under challenging conditions involving noisy training inputs, as highlighted in Table 9.

We observe relative error increases of 22%, 47%, and 28% for CoNO, LSM, and FNO, respectively. Here, CoNO outperforms all the models. Furthermore, under 0.5% data noise conditions, our findings indicate relative error increases of 62%, 186%, and 45% for CoNO, LSM, and FNO, respectively. Here, it performs significantly better than LSM but poorer than FNO. However, it should be noted that the absolute performance of CoNO in relation to FNO is considerably better. Thus, it can be argued that CoNO is robust against noise at least as much as FNO, if not better and better LSM, which is the SOTA model.

Table 9: Neural Operators performance comparison on Darcy Flow under different noise Levels in the training dataset. "/" indicates poor ℓ_2 error performance.

Noise %	UNET	FNO	MWT	UNO	FFNO	HTNET	LSM	CoNO
0 %	0.0080	0.0108	0.0082	0.0113	0.0083	0.0079	0.0065	0.0050
0.001 %	0.0094	0.0114	0.0089	0.0115	0.0089	0.0087	0.0085	0.0056
0.01 %	0.0105	0.0137	0.0097	0.0121	0.0095	0.0097	0.0087	0.0058
0.1 %	0.0113	0.0139	0.0125	0.0126	0.0106	0.0124	0.0096	0.0061
0.5 %	/	0.0157	0.0135	0.0138	0.0125	0.0148	0.0186	0.0081

F.3 Out of Distribution Generalization

In this study, we conducted extensive experiments utilizing the Navier-Stokes dataset, training our model with a viscosity coefficient set to 10^{-5} . Subsequently, we rigorously assessed the out-of-distribution generalization capabilities by subjecting the trained model to a viscosity coefficient of 10^{-4} , as depicted in Table 10. Our empirical observations consistently demonstrate that the CoNO model exhibits a notably superior generalization performance, showcasing an impressive increment of 64.3% compared to the FNO model’s performance. Furthermore, our findings underscore the critical importance of capturing latent variable information, a task effectively accomplished by the UNET architecture, particularly exemplified by the Latent Spectral Operator. Significantly, LSM outperforms all other operators, including CoNO, emphasizing its role in enhancing generalization capabilities in fluid dynamics modeling.

Table 10: Neural Operators performance comparison on the Navier-Stokes Benchmark Under Out of distribution performance. Model is trained on NS viscosity coefficient $1e^{-5}$ and tested on NS viscosity coefficient $1e^{-4}$. "/" indicates poor ℓ_2 error performance.

NS Viscosity Coefficient	UNET	FNO	MWT	UNO	FFNO	HTNET	LSM	CoNO
$1e^{-5}$	0.1982	0.1556	0.1541	0.1713	0.2322	0.1847	0.1535	0.1287
$1e^{-4}$	/	0.6621	0.5864	0.5436	0.5606	0.4888	0.1887	0.2321

F.4 Effect of Number of Layers

We conducted experiments to analyze the relationship between the number of layers and performance, in comparison to FNO, on the Darcy flow dataset. Our findings, presented in the table below, reveal that performance initially improves with increased layers in FNO. However, a significant drop in performance occurs due to the vanishing gradient problem. Importantly, our method consistently avoids the vanishing gradient problem even with an increase in the number of layers, as shown in Table 11.

Table 11: Neural Operators performance comparison on Darcy Benchmark under different numbers of layers.

Number of Layers	2	4	6	8
FNO	0.0114	0.0108	0.0087	0.0098
CoNO	0.0066	0.0052	0.0053	0.0052

F.5 Long Term Prediction

In further substantiating our evidence regarding the enhanced stability of CoNO in long-horizon predictions, we conducted an additional experiment utilizing the Navier Stokes model with a viscosity coefficient of 10^{-4} . Here, we performed forecasts for the subsequent ten steps based solely on the preceding ten observations and extrapolated the results over ten more steps. The outcomes of this experiment are presented in the tables below. Our findings indicate that although not explicitly trained for predicting the subsequent 20 timestamps, CoNO consistently outperforms LSM and FNO in extrapolating beyond the prediction horizon. This observation underscores the heightened stability and robustness of CoNO in long-horizon prediction tasks as shown in Table 12.

Table 12: A comparative analysis of the performance of Neural Operators on the Navier-Stokes equations, with a viscosity coefficient of 10^{-4} , involves training models to predict the subsequent 10 timestamps based on the preceding 10 timestamps. Subsequently, the extrapolated results are utilized to forecast the subsequent 10 timestamps.

Neural Operator	$T = 5$	$T = 10$	$T = 15$	$T = 20$
FNO	0.028	0.050	0.17	0.34
LSM	0.065	0.13	0.24	0.38
CoNO	0.020	0.045	0.14	0.31

F.6 Data Efficiency

As shown in Table 13, the performance of CoNO is superior, showcasing its competitive capabilities comparable to the second-best operator LSM when trained on 60% of the available data. Remarkably, across diverse training dataset ratios, CoNO consistently surpasses all other operators, emphasizing its remarkable data efficiency compared to state-of-the-art (SOTA) operators. This observation underscores the efficacy and robustness of CoNO across varying training scenarios, positioning it as a noteworthy solution in the realm of operator-based learning. With a data ratio of 0.6, we observed relative error increases of 34%, 44%, and 35% for CoNO, LSM, and FNO, respectively. Thus, it is evident that our approach consistently outperforms the second-best operator, LSM, across various ratio settings. Further, the absolute performance of CoNO is significantly better than that of FNO.

Table 13: Neural Operators performance comparison on Darcy Benchmark under different training dataset ratios. "/" indicates poor ℓ_2 error performance.

Ratio	UNET	FNO	MWT	UNO	FFNO	HTNET	LSM	CoNO
0.2	/	0.2678	0.2854	0.2734	0.2573	0.2564	0.2465	0.2234
0.4	/	0.0176	0.0165	0.0183	0.0153	0.0145	0.0138	0.0105
0.6	0.1234	0.0146	0.0113	0.0153	0.0142	0.0105	0.0094	0.0067
0.8	0.0107	0.0122	0.0096	0.0134	0.0095	0.0094	0.0082	0.0056
1.0	0.0080	0.0108	0.0082	0.0113	0.0077	0.0079	0.0065	0.0050

F.7 Efficiency

To clearly compare efficiency across different models, we standardize the input by using a regular grid with a resolution of 64×64 . This section analyzes model parameters, training time, and inference time complexity for various neural operators applied to the Darcy Flow benchmark dataset in fluid physics. The goal is to highlight these operators' computational efficiency and effectiveness in modeling fluid flow phenomena, as detailed in Table 14.

G Limitation and Future Work

To enhance our understanding of CoNO, it is crucial to thoroughly explore its mathematical and algorithmic principles. Future research could extend proposed approach by incorporating additional branches, like using multiple kernels or channels in CNNs, to achieve a more comprehensive spatial-frequency distribution. Critical areas for further investigation include determining the optimal number of branches, the best initialization strategies for fractional orders, and the efficient implementation of fractional convolution within transformers. We aim to uncover the latent space's learning mechanisms and build a solid theoretical foundation for complex operators. Our research highlights several key challenges that need careful investigation, including refining

Table 14: The evaluation of parameters, training time and inference time complexity across various neural operators on the Darcy Flow benchmark dataset in the domain of Fluid Physics for one data per iteration.

Neural Operator	# Params (M)	GPU Memory (MB)	Training (s/iter)	Inference (s/iter)
UNET	4.332	1171	0.0321	0.025
FNO	2.368	1137	0.0202	0.017
FFNO	0.218	1089	0.0303	0.025
HT-NET	3.285	1175	0.0406	0.032
SWIN	0.538	1135	0.0615	0.046
GALEKIN	6.319	1233	0.0252	0.020
MWT	3.103	1145	0.0615	0.042
GNOT	5.202	1507	0.0825	0.063
LSM	2.002	1409	0.0353	0.020
CoNO	2.432	1208	0.0312	0.024

initialization procedures for fractional orders, designing streamlined architectures for complex neural operators, developing equivariant complex operators, and understanding the role of the Fractional Fourier Transform (FrFT) in the continuous dynamics of complex systems. Additionally, our work raises questions about creating foundational models for Partial Differential Equations (PDEs). These research directions offer opportunities to further understand CoNO and contribute to the broader field of Scientific Machine Learning (SciML).

H Broader Impact

This paper introduces innovative tools to revolutionize scientific machine learning (SciML). By integrating Complex Neural Networks (CVNNs) and the Fractional Fourier Transform (FrFT) into the Neural Operator framework, we offer a novel approach to addressing the complex challenges of partial differential equations (PDEs), particularly Fractional PDEs, which lack explicit differential forms and are common in natural phenomena [1, 40]. Our research has significant implications for diverse fields such as biology, physics, and civil engineering, addressing a crucial scientific problem and paving the way for transformative advancements in interdisciplinary problem-solving. There is no serious ethical issue of the proposed methodology.